Journal of Applied Physics

RESEARCH ARTICLE | JANUARY 23 2026

Metrology for femtosecond pulsed x-ray heating in diamond anvil cell experiments at the European XFEL: Revisiting the iron phase diagram up to 150 GPa

Hélène Ginestet ; Rachel J. Husband ; Nicolas Jaisle ; Eric Edmund ; Zuzana Konôpková ; Cornelius Strohm ; Madden S. Anae ; Daniele Antonangeli ; Karen Appel ; Orianna B. Ball ; Marzena Baron ; Silvia Boccato ; Khachiwan Buakor ; Julien Chantel ; Hyunchae Cynn ; Anand P. Dwivedi ; Heinz Graafsma ; Egor Koemets ; Torsten Laurus; Hauke Marquardt ; Bernhard Massani ; James D. McHardy ; Malcolm I. McMahon ; Vitali Prakapenka ; Jolanta Sztuk-Dambietz; Minxue Tang ; Tianqi Xie ; Zena Younes ; Ulf Zastrau ; Alexander F. Goncharov ; Clemens Prescher ; Agnès Dewaele ; R. Stewart McWilliams ; Guillaume Morard ; Sébastien Merkel

J. Appl. Phys. 139, 045901 (2026)
https://doi.org/10.1063/5.0303953
CHORUS

Journal of Applied Physics ARTICLE pubs.aip.org/aip/jap

Metrology for femtosecond pulsed x-ray heating in diamond anvil cell experiments at the European XFEL: Revisiting the iron phase diagram up to 150 GPa

Cite as: J. Appl. Phys. **139**, 045901 (2026); doi: 10.1063/5.0303953
Submitted: 25 September 2025 · Accepted: 15 December 2025 ·
Published Online: 23 January 2026

Hélène Ginestet,[1,a)] Rachel J. Husband,[2] Nicolas Jaisle,[3,4] Eric Edmund,[5,b)] Zuzana Konôpková,[6] Cornelius Strohm,[2] Madden S. Anae,[7] Daniele Antonangeli,[8] Karen Appel,[6] Orianna B. Ball,[4] Marzena Baron,[9] Silvia Boccato,[8] Khachiwan Buakor,[6] Julien Chantel,[1] Hyunchae Cynn,[10] Anand P. Dwivedi,[5,6] Heinz Graafsma,[2] Egor Koemets,[11,12] Torsten Laurus,[2] Hauke Marquardt,[11] Bernhard Massani,[4] James D. McHardy,[4] Malcolm I. McMahon,[4] Vitali Prakapenka,[13] Jolanta Sztuk-Dambietz,[6] Minxue Tang,[2] Tianqi Xie,[7,14] Zena Younes,[4] Ulf Zastrau,[6] Alexander F. Goncharov,[5] Clemens Prescher,[15] Agnès Dewaele,[16,17] R. Stewart McWilliams,[4] Guillaume Morard,[3,8] and Sébastien Merkel[1,c)]

AFFILIATIONS

[1]Univ. Lille, CNRS, INRAE, Centrale Lille, UMR 8207—UMET—Unité Matériaux et Transformations, F-59000 Lille, France
[2]Deutsches Elektronen-Synchrotron (DESY), Notkestr. 85, 22607 Hamburg, Germany
[3]ISTerre, Université Grenoble Alpes, CNRS, Grenoble, France
[4]SUPA, School of Physics and Astronomy, and Centre for Science at Extreme Conditions (CSEC), The University of Edinburgh, Peter Guthrie Tait Road, Edinburgh EH9 3FD, United Kingdom
[5]Earth and Planets Laboratory, Carnegie Institution for Science, 5251 Broad Branch Rd., Washington, DC 20015, USA
[6]European XFEL, Schenefeld, Germany
[7]Department of Geosciences, Stony Brook University, Stony Brook, New York 11794-2100, USA
[8]Sorbonne Université, Muséum National d'Histoire Naturelle, UMR CNRS 7590, Institut de Minéralogie, de Physique des Matériaux et de Cosmochimie (IMPMC), Paris, France
[9]Sorbonne Université, CNRS, Laboratoire Chimie de la Matière Condensée de Paris (LCMCP), 4 place Jussieu, 75005 Paris, France
[10]Lawrence Livermore National Laboratory, Physical and Life Science Directorate, Livermore, California 94550, USA
[11]Department of Earth Sciences, University of Oxford, 3 South Parks Road, OX1 3AN Oxford, United Kingdom
[12]Diamond Light Source, Diamond House, Didcot OX11 0DE, United Kingdom
[13]Center for Advanced Radiation Sources, The University of Chicago, Chicago, Illinois 60637, USA
[14]Geological Sciences, University of Saskatchewan, Saskatoon, Saskatchewan S7N5E2, Canada
[15]Institute of Earth and Environmental Sciences—Geomaterials and Crystalline Materials, Albert-Ludwigs Universität Freiburg, Hermann-Herder Str. 5, 79104 Freiburg, Germany
[16]CEA, DAM, DIF, 91297 Arpajon, France
[17]Université Paris-Saclay, CEA, Laboratoire Matière en Conditions Extrêmes, 91680 Bruyères-le-Châtel, France

[a)]**Author to whom correspondence should be addressed:** helene.ginestet@univ-lille.fr
[b)]**Present address:** Institüt für Mineralogie, Universität-Münster, 48149 Münster, Germany
[c)]**Email address:** sebastien.merkel@univ-lille.fr

ABSTRACT

The development of pulsed intense x-ray sources, such as free electron laser, offers new avenues for high pressure experiments. Here, we study the feasibility and metrology of x-ray heating in diamond anvil cells at the European x-ray free electron laser. This method enables one to volumetrically heat the sample while inhibiting chemical migration and probing the crystallographic structure of the sample throughout the heating with a high repetition rate. We focus our study on iron, whose phase diagram is well established up to 100 GPa, to explore the possibilities and limitations of this technique. We volumetrically heat iron samples at starting pressures ranging from 10 to 138 GPa, using the x-ray beam pulsed at 4.5 MHz in a serial pump-and-probe experimental design. Experimental challenges arise from temperature gradients within the sample, changes in temperature at the 100 ns timescale, the difficulty of direct temperature estimates, the effect of thermal pressure, and the presence of metastable crystallites due to rapid cycles of heating and cooling. Hence, we develop a multi-crystal-like data processing method that allows us to account for sample heterogeneity in probed conditions. We then calibrate our measurements using known physical properties of iron under pressure. Thermal pressure in our experiments increases from 4% of the isochoric prediction at 10 GPa to 23% at 138 GPa, and we show that our data are in agreement with most previous observations of iron in this pressure range. The method can now be implemented at higher pressures and temperatures and on materials with unknown phase diagrams.

 https://doi.org/10.1063/5.0303953

I. INTRODUCTION

The study of materials under extreme conditions has numerous applications in both material[1,2] and planetary sciences.[3] The development of extreme conditions studies depends on joint advances in technologies to reach high pressure and high temperature conditions and *in situ* sample characterization methods.[4] Noteworthily, the increasing brilliance of x-ray sources in the last 20 years has allowed researchers to perform *in situ* x-ray diffraction and spectroscopy measurements of constantly improving quality.[2] Among the different techniques commonly used to generate high pressure (*HP*) conditions, the diamond anvil cell (DAC) enables the confinement of samples at static high pressures for periods of time exceeding days or even months. Coupled with laser-heating,[5–8] the sample can be statically compressed and heated to high temperatures (*HT*) for up to several hours, enabling studies of thermodynamic equilibrium and properties at the Earth's mantle and core conditions.[9–13] However, intrinsic difficulties include pressure (P) and temperature (T) gradients,[14–16] chemical contamination from the diamond anvil and surrounding media,[8,17–19] and problems with the process of laser-heating itself, such as for samples with high reflectivity.[20] To overcome some of these hindrances, studies have been conducted with pulsed laser-heating.[6,7,21] However, existing synchrotron facilities generally require the collection of x rays from many pulsed heating events to achieve a good signal to noise ratio, which still leads to experimental timescales at which chemical migration and contamination can readily occur.[22]

New generation x-ray sources, such as X-ray free electron lasers (XFEL), offer new opportunities in this field. Their short (<100 fs) but brilliant x-ray pulses enable high resolution sample characterization using x rays without cumulative measurements.[23–27] The European XFEL (EuXFEL) is unique in that its pulsed beam allows time-resolved measurements with a frequency up to 4.5 MHz.[23,25] This feature has been used to develop new pump and probe techniques to induce volumetric heating (heating of the bulk of the sample as opposed to surface heating, using an infra-red laser, for example) and probe the sample state using x-ray diffraction. Previous studies have shown that such a high rate of x-ray exposure can lead to cumulative sample heating up to several thousands of K or more depending on the sample composition.[28–30] The method can, hence, be used, in combination with static pressures generated by DAC, to explore HP/HT phase diagrams of materials. However, this new ultrafast heating and characterization process requires the development of new analysis methods, both to handle the large volume of data generated and to ensure accurate metrology, particularly in evaluating the actual sample pressure and temperature.

Here, we focus our study on a well-studied material, pure iron (Fe). As Fe is the main constituent of planetary cores, its phase diagram (see Fig. 1), equations of state and melting curve have been extensively studied, both experimentally and by simulations. Starting in a body centered cubic (bcc or α-Fe) phase at ambient conditions, it transforms into a face centered cubic (fcc or γ-Fe) phase upon heating. Below 5 GPa, it transforms into a bcc (δ-Fe) phase before the melting temperature,[36] while retaining the fcc phase until melting at higher pressures. When compressed, α-Fe transforms into a hexagonal close-packed (hcp or ε-Fe) phase with a significant pressure-induced hysteresis around 12 GPa at room temperature (*RT*).[37,38] The α–γ–ε triple point is situated at 9.2 ± 1.3 GPa and 730 ± 50 K (Ref. 31 and references therein). The stability domain of γ-Fe extends up to the γ–ε–liquid triple point. Although earlier studies placed the γ–ε–liquid triple point around 60 GPa and 2800 K,[39,40] the current agreement places it closer to 100 ± 10 GPa with a T ranging from 2800 to 3712 K depending on the considered study.[17,32,33,41–44] From the triple point and up to 200 GPa, hcp is stable from *RT* up to melting. Some studies argue that the hcp structure is stable from *RT* until melting, even above 1.5 TPa,[45,46] while others argue that a bcc phase would become stable below the melting curve above 200 GPa.[27,47,48] The melting curve remains a topic of study with discrepancies at the Earth inner core boundary (330 GPa) reaching 900 K between the low $T_m = 5800$ K reported in Ref. 40 and the highest $T_m = 6700$ K reported in Ref. 49.

In this paper, we explore the phase diagram of Fe using the pulsed beam of the European XFEL in order to validate the method of pump and probe x-ray heating in the diamond anvil cell on a well-studied phase diagram, refine the data analysis procedures,

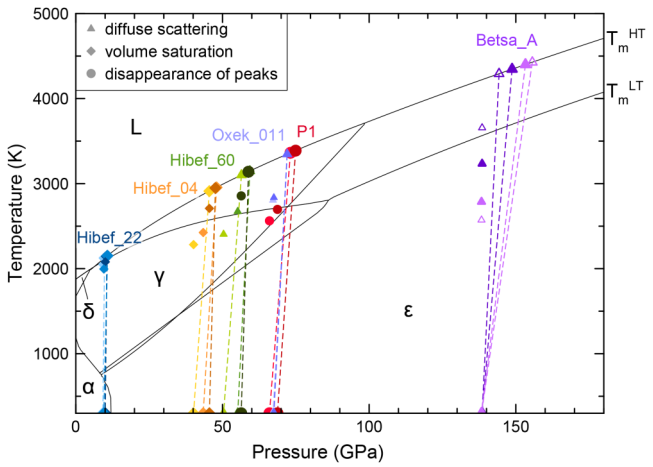

FIG. 1. *P–T* pathways during heating superimposed on iron phase diagram. Stability domain limits for the α and δ phases are from Ref. 31. The high temperature γ–ε and melting (T_m^{HT}) curves are from Ref. 32. The low temperature γ–ε and melting (T_m^{LT}) curves are from Refs. 33–35. Symbols represent the detection method and conditions at which melting was observed (see Sec. III C). The smaller and unconnected symbols are conditions evaluated without thermal pressure corrections. The larger connected symbols include thermal pressure corrections. Colors correspond to different samples, whose names are indicated on the figure: Hibef_22, Hibef_04, Hibef_60, Oxek_011, P1, and Betsa_A (see Table I for DAC details and *P* conditions).

and develop a metrology to determine pressure and temperature in such experiments. We will focus our study mainly below 100 GPa, where the phase diagram is less controversial for Fe, and exploit this new experimental facility to explore the phase diagram of pure Fe up to 155 GPa at high temperature.

This article is organized as follows. In Sec. II, we present the sample preparation and EuXFEL experimental protocol. Section III is devoted to the data processing procedures: analysis of 4.5 MHz x-ray diffraction images, criteria for phase identification, and the procedure to evaluate sample pressure and temperature conditions. Section IV then presents the effect of x-ray intensity on observed phases and sample conditions, the stability of the observed iron phases, thermal pressure, and gradients in sample conditions. The observed phases are in agreement with the phase diagram based on the current literature and, based on known equations of state of iron, we propose calibration for thermal pressure in such experiments.

II. EXPERIMENT

A. Samples

The results presented in this paper are from the No. 3063 community proposal at the EuXFEL. The Fe samples were prepared from a 5 μm thick iron foil of 99.85% purity from GoodFellow (Product No. FE00-FL-000100) and cut into disks using a femtosecond laser. Fe disks were then loaded into sample chambers in Re gaskets with potassium chloride (KCl) as a pressure transmitting medium (PTM), except for the Oxek_011 cell, for which the PTM was fused SiO_2 powder from Sigma-Aldrich (CAS No. 112945-52-5). Cells loaded with KCl were placed in an oven for ~12 h to dry the salt before being closed and compressed. Details on diamond anvil cells type, samples, and diamond dimensions are provided in Table I. The samples were characterized before and after the EuXFEL experiments using synchrotron x-ray powder diffraction at the beamline P02.2, PETRA III, DESY, Hamburg. A $2 \times 2\,\mathrm{mm}^2$ beam with an incident energy of 42.7 keV ($\lambda = 0.2905$ Å) in combination with a Perkin-Elmer XRD 1621 flat panel detector with 2048×2048 pixels of $0.2 \times 0.2\,\mathrm{mm}^2$ placed at a distance of 416 mm from the sample was used to estimate starting and final pressures and assess the quality of the DAC loadings. During post-screening after the EuXFEL experiments, 2D diffraction maps were performed by collecting XRD diffraction images at every points over a grid in the horizontal and vertical direction, with a step size of 5 or 10 μm (see Appendix B, Fig. 16). Post-screening XRD maps confirm the absence of other phases, such as iron carbides, which would occur due to carbon contamination from the diamond anvils.

B. XFEL experiment

We used the High Energy Density (HED) instrument of the EuXFEL[26] using a layout similar to that described in Ref. 25 in interaction chamber 2. The x-ray beam is pulsed at 4.5 MHz. Those pulses are fired on the sample in trains of 352 pulses. Coupled with the Adaptive Gain Integrating Pixel Detector (AGIPD),[50] which can acquire up to 352 diffraction patterns sequentially at this frequency, this allows for a time-resolved structural analysis of the sample over 78 μs. A run comprises a single train on the sample and the associated diagnostic measurements.

Each time the sample is exposed to an x-ray pulse, the pulse is partially absorbed by the electron cloud,[51] causing the sample to heat on a very short timescale. The sample then cools and is probed upon cooling by the following x-ray pulse, 221.5 ns later in the train. The corresponding schematic sample temperature evolution with time is shown in Fig. 2.

Figure 3 shows a simplified schematic of the setup used in this experiment. The x-ray energy was measured to be 18.08 keV ($\lambda = 0.6858$ Å) using the HIREX-II spectrometer.[25,52] The intensity of individual pulses varies within each train and from train to train. The pulse energies of all 352 pulses were derived from measurements of scattered light from a thin diamond window by fast diodes placed before the interaction point, calibrated to absolute pulse energies using X-ray gas monitors (XGMs)[53] prior to the experiment. The XFEL focal spot size on the sample was measured to be 3–5 μm full-width half maximum based on foil imprint analysis.[51] Attenuators can be placed in the path of the x-ray beam to control the intensity of x rays transmitted to the sample. In the paper, we will refer to x-ray transmission (% tr), calculated as a ratio of the transmitted beam intensity with respect to that of the full beam. Each x-ray pulse deposits energy into the sample. For low x-ray transmission, heating due to x-ray absorption does not exceed heat loss due to thermal diffusion and sample heating is small. At higher transmission, x-ray absorption heats the sample faster than thermal diffusion allows the sample to cool, which can induce significant heating and phase transitions.

TABLE I. List of samples with results presented in this paper. For each, the table presents the name and type of the DAC, the pressure transmitting medium we used, the diameters of the diamond culet, sample chamber, and Fe samples, and the corresponding run numbers. Pressure varies during the experiment due to pressure gradients and repeated cycles of sample heating with the XFEL. The table, hence, reports the pressure at the start and end of the experiment, as well as the minimum and maximum pressures reached during the run. Cell Hibef_04 was loaded with two samples of 50 μm diameter.

DAC		Pressure medium	Diameters (μm)			Pressure (GPa)				Run numbers
Name	Type		Culet	Fe sample	Chamber	Start	End	Min.	Max.	
Hibef_22	Symmetric	KCl	300	75	120	9.5	10.1	3.6	10.1	0036–0056
Hibef_04	Symmetric	KCl	300	50 (2×)	115	38	42	32	46	0005–0035
Hibef_60	Symmetric	KCl	300	65	120–145	52	68	47	68	0564–0617
Oxek_011	Symmetric	SiO_2	200	50	80	69	62	55	64	0057–0080
P1	Symmetric	KCl	250	30	75	80	72	66	84	0413–0436
Betsa_A	Le Toullec	KCl	100	30	45–49	148	131	127	150	0437–0471

The AGIPD detector, located outside the interaction chamber behind an Al window, was used to collect angle-dispersive X-ray diffraction (XRD), with a 2θ Bragg angular coverage between 9° and 30°. The sample-detector distance of 356.45 mm and other integration parameters have been calibrated against the XRD pattern of a Cr_2O_3 standard collected during the experiment.

For each DAC, we tested the different x-ray transmission levels on a first position on the sample to determine what transmission induced a visible change in the sample crystallographic unit cell volume and structure (Fig. 4). Low x-ray transmissions have no visible effect on the sample. Increasing x-ray transmissions induces sample heating (indicated by thermal expansion of the unit cell) and, potentially, phase transitions (new peaks) and melting. High-transmission runs were alternated with low-transmission runs at fresh sample positions to compare the sample structure before, during, and after heating.

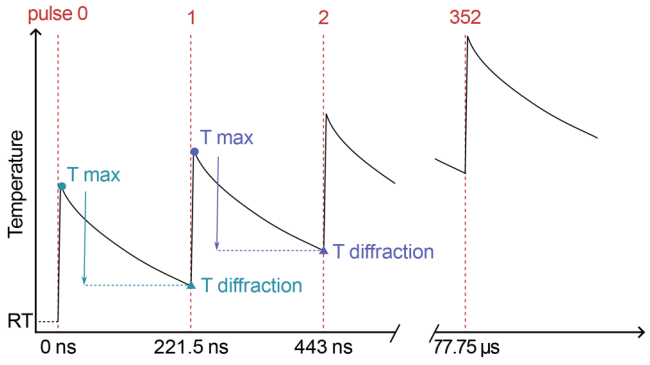

FIG. 2. Schematic representation of the expected sample temperature evolution as a function of time. Subsequent to the almost immediate diffraction of the incoming x-ray pulse, part of the x-ray energy induces a volumetric elevation in temperature. Temperature then decreases by diffusion, until the next pulse arrives onto the sample. The drop between the peak temperature and the one at which the diffraction is taken increases with the global temperature and can reach several thousands of K according to finite element modeling[28] (see Appendix D).

III. DATA PROCESSING

A. Time series measurements

The diffraction patterns are first analyzed using Dioptas.[54] Azimuthal integration of the XRD data yields a 1D pattern of the intensity as a function of 2θ. Diffraction patterns collected from the 352 successive pulses in a train are then stacked to build an image depicting the evolution of diffraction patterns with time, or pulse number, allowing for a quick assessment of the observed phases and their crystallographic features. Figure 4 shows the time series of four runs on the P1 cell at 75 ± 9 GPa, using different x-ray transmissions. At low x-ray transmission [0.1% tr, Fig. 4(a)], no thermal expansion is observed in the sample at probe time, as evidenced by the lack of variation in the 2θ position of the hcp-Fe diffraction lines. These data can be used as a diffraction pattern reference for the analysis. The amount by which x-ray transmission is increased allows one to control the magnitude of sample heating. Figure 4(b) shows the results of x-ray diffraction with 1% tr in which thermal expansion can be observed. As transmission increases, the temperature in the sample builds further, which can lead to phase transitions, whether solid–solid, as shown in Fig. 4(c) with 2.5% tr (hcp to fcc transition), or even solid–liquid, as shown in Fig. 4(d) at 4.5% tr (hcp to fcc to melting). With further increased x-ray transmission, the same transformation is reached

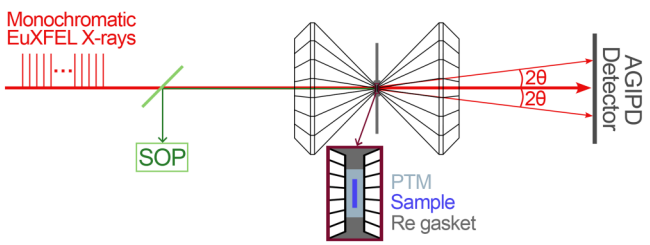

FIG. 3. Experimental layout. The starting material is a 5 μm thick foil of pure Fe. The pressure transmitting medium is KCl or SiO_2. The detector is perpendicular to the incoming x-ray beam and the compression axis of the DAC, and parallel to the surface of the sample. X-ray pulses, lasting ~25 fs, arrive at a frequency of 4.5 MHz, leading to diffraction patterns every 221.5 ns. A streak optical pyrometry (SOP) system is set up upstream of the DAC.[28]

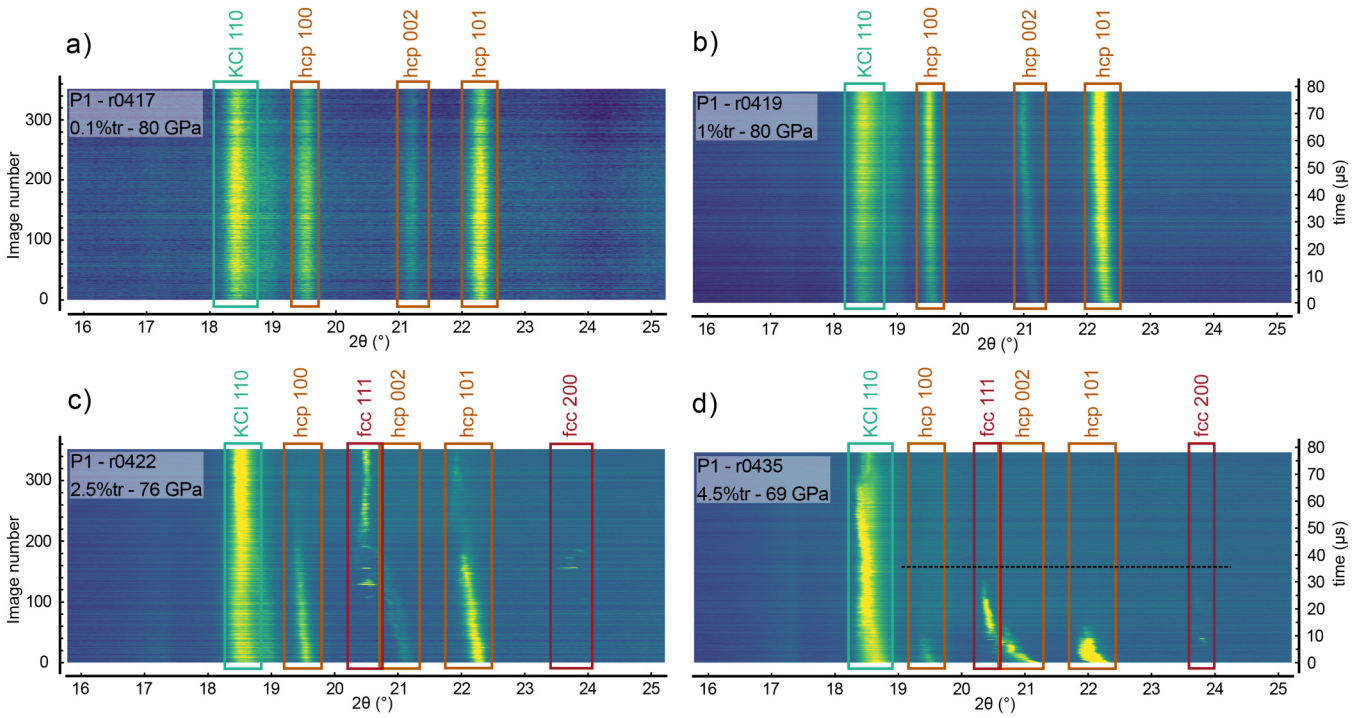

FIG. 4. Azimuthally integrated x-ray diffraction images stacked as a function of time or frame (diffraction image) number for several runs on the P1 cell (75 ± 9 GPa). Time goes from bottom (frame 1 at 0 μs) to top (frame 352 at 77.7 μs). (a) Run r0417 (0.1% tr). The sample is in the hcp structure during the whole run and does not show any sign of thermal expansion. (b) Run r0419 (1% tr). The sample is in the hcp structure during the whole run and shows some thermal expansion, expressed as a shift of the diffraction peaks toward lower 2θ angles. (c) Run r0422 (2.5% tr). The sample starts in the hcp structure and transforms into the fcc structure starting from frame (or image number) 106 at 23.26 μs. The intensity of the hcp diffraction peaks decreases when fcc iron appears, but 100 and 101 hcp peaks remain visible until the end of the run. (d) Run r0435 (4.5% tr). The sample, initially in the hcp structure, starts to transform into fcc at frame 15 at 3.10 μs. At frame 76 at 16.61 μs, it is fully transformed to fcc. All diffraction peaks from solid Fe disappear on frame 162 at 35.66 μs (dotted black line).

earlier in the pulse train. For instance, the hcp to fcc transition starts at 23.31 μs in run r0422 with 2.5% transmission and at 3.11 μs for run r0435 with 4.5% transmission.

B. Detecting phase transitions

Phase identification is first performed on integrated patterns time series (e.g., Fig. 4) in which we identify α-, γ-, or ε-Fe. The exact timing of the appearance of a new phase is then refined by searching for the first appearance of individual diffraction spots directly in the 2D diffraction images. Note, however, that 111_{fcc} and 002_{hcp} overlap and can be hard to assign unambiguously. The concomitant observation of 200_{fcc}, for instance, is then used to confirm the presence of γ-Fe in the sample.

Figure 5 shows an example from run r0037, from cell Hibef_22 at 10 GPa. During XFEL irradiation, the diffraction peak from α-Fe shifts to lower angles due to thermal expansion during heating. 100_{hcp} and 101_{hcp} peaks appear, followed by 111_{fcc} and 200_{fcc}, after 4.21 and 9.75 μs, respectively. Note that 002_{hcp} is not clearly observed due to grain orientations caused by uniaxial stress

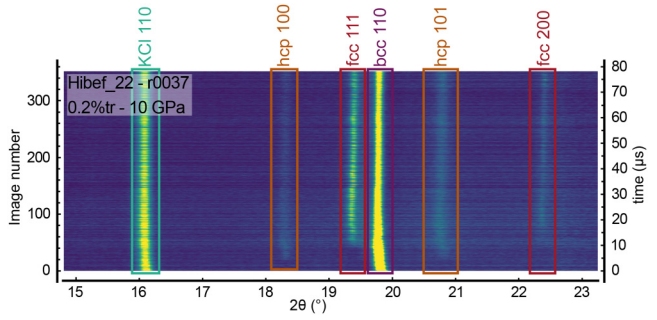

FIG. 5. Azimuthally integrated x-ray diffraction images stacked as a function of time or frame number for run r0037 (0.2% tr) of cell Hibef_22 at 10 GPa. The sample starts with Fe in the bcc structure. The bcc unit cell expands with heating, then hcp-Fe 100 and 101 peaks appear on frame 20 at 4.21 μs, and fcc-Fe peaks appear on frame 45 at 9.75 μs. All three phases are visible simultaneously until the end of the run due to thermal gradients and phases metastability.

and an overlap with 110_{bcc}. This sequence of phase transitions can be explained in view of the proximity of the P–T conditions with the α–γ–ε-Fe triple point at 9.2 ± 1.3 GPa and 730 ± 50 K (Ref. 31 and references within).

C. Evidence for melting

The criterion for detecting melting in DAC experiments has been a topic of debate for decades,[8,17,19,55] with the appearance of a diffuse scattering signal often considered as an unambiguous bulk signature of melting.[32] A diffuse scattering signal from molten Fe is sometimes observed (e.g., Appendix C, Fig. 17), but not consistently due to the detector background. Moreover, before the total melting of the sample, the solid diffraction signal dominates the diffraction as the large beam with long tails probes a significant portion of cold, external sample.

In some cases [e.g., Fig. 4(d)], we observe the disappearance of all Fe diffraction peaks, indicating that there are no more solid Fe grains probed by the x-ray beam. In other cases, we observe a clear saturation in the 2θ position of the diffraction peaks of the high-temperature phase, contrasting sharply with the 2θ shift caused by thermal expansion (Fig. 6). This saturation is also sometimes observed for hcp peaks when a transformation into fcc occurs [e.g., Fig. 4(d)]. Saturation in the volume shift occurs when phase transformations are observed during serial pump and probe experiments due to the presence of temperature gradients.[30,51]

In this study, due to intermittent detection of a diffuse scattering signal, we also used the disappearance of the sample diffraction peaks for the HT phase and the saturation in the position of these peaks as evidence for melting. We then extracted the largest unit cell volume of the HT solid phase of Fe observed during the run, which was considered to originate from the hottest solid portion of the sample and, hence, at a temperature just below that of the melting line. This maximum solid-state volume was then compared, in combination with an equation of state, to the expected temperature at melting. The different criteria used for detecting melting for each run studied in this paper are presented in Table II.

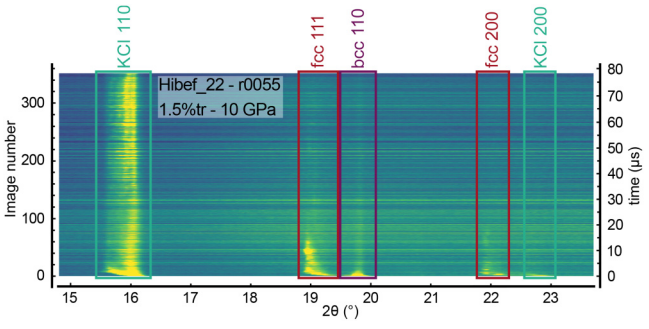

FIG. 6. Azimuthally integrated x-ray diffraction images stacked as a function of time or frame number for run r0055 (1.5% tr) of cell Hibef_22 at 10 GPa. The sample starts in the bcc structure. Fcc peaks appear at frame 2 (0.22 μs) and shift toward lower 2θ as the sample heats. This increase in unit cell volume stops abruptly, corresponding to a sharp saturation in volume on frame 8 (1.55 μs). Both bcc and fcc solid phases are observed all along the run, indicating temperature gradients in the region probed by x rays. The diffraction intensity decreases drastically starting at frame 7 (1.33 μs) for the bcc phase and frame 60 (13.07 μs) for the fcc phase, suggesting a conversion of most of the sample into fcc then melt. The remaining peaks are at positions corresponding to lower temperature and probably originate from grains probed by the tails of the x-ray beam. As shown by the shape of the KCl peak, the PTM is significantly heated as well and exhibits a volume saturation corresponding to its own melting point, with a naturally larger range of conditions visible in the peak distribution.

D. Sample structure and microstructure

Due to the nature of successive cycles of heating and cooling (Fig. 2) every 221.5 ns, the sample microstructure can evolve drastically from frame to frame. Figure 7, for instance, shows three successive frames from run r0435 of cell P1 at 69 GPa. The fcc-Fe diffraction spots are sharp and show evidence of recrystallization between frames. The rapid recrystallization of fcc-Fe indicates that this portion of the sample is close to the melting temperature or has melted and then crystallized during quenching between pulses. In contrast to diffraction from fcc-Fe, diffraction patterns from hcp-Fe and KCl only weakly evolve over this time span.

Finite element modeling of this run was performed according to the procedure described in Refs. 56 and 57 and in Appendix D. Figure 8(a) shows the measured x-ray pulses intensities (top) and calculated temperature evolution with time at the center of the sample and at the sample–PTM interface. Figure 8(b) shows the shape of the x-ray pulse. Figure 8(c) shows the spacial temperature distribution at the hot state created by the 42nd pulse. While the temperature at the center of the sample exceeds 3800 K, it decreases to less than 1200 K only 5 μm away from the center in the radial direction. The axial temperature gradient in the sample is much smaller and decreases when moving away from the DAC axis. Figure 8(d) presents a map of the sample density, which is used to highlight the domain of each stable phase based on the known phase diagram and the calculated conditions. The liquid portion consists of a cylinder of $\sim$1.3 μm radius centered around the x-ray beam, surrounded by a 0.5 μm thick layer of fcc-Fe, followed by hcp-Fe. When the next pulse arrives, the sample has cooled below the melting temperature [see Fig. 8(a), inset, and Fig. 9], and only fcc and hcp will be probed. However, later in the run, the three phases will co-exist, be probed simultaneously, and be observed in the diffraction image due to the extended nature of the x-ray beam[51] [Fig. 8(b)]

Integrated powder diffraction patterns fail at describing these gradients of conditions inside the sample. In fact, spots from grains at different temperatures tend to overlap and can be interpreted as originating from a single material. In order to better describe pressure and temperature gradients within the sample, a Python script, similar to that described in Ref. 59, was developed to detect and map diffraction spots from individual grains directly from the 352 images in the pulse train.

The script extracts the 2θ and azimuthal positions of individual Bragg spots from every frame, allowing for the calculation of the phase unit cell distribution over time. In most samples, unit cell volumes for α-Fe and γ-Fe individual grains are then calculated from the 110 and 111 reflections, respectively. In this analysis, other peaks, such as 200_{fcc} or 002_{hcp}, are not considered because they do not always appear consistently from frame to frame

TABLE II. Summary of runs presented in this study. For each run, the table shows the cell for which it was measured, the pressure determined from the first frame of the run, the run number, the x-ray transmission used (x-ray tr.), the range of corresponding pulse x-ray energies, the observed phase transitions and time in the run at which they start/end. The criteria used to determine melting are also indicated. *V* sat.: unit cell volume saturation, that is visible saturation of the thermal expansion induced shift of the diffraction peak; diff. scatt.: diffuse scattering visible in the diffraction pattern; no peak: disappearance of diffraction peaks from the sample.

Cell	300 K *P* (GPa)	Run number	X-ray tr. (%)	X-ray En. (μJ)	Observations	Time of phase change (μs)
Hibef_22	10	r0037	0.2		α–γ–ε triple point	9.3
	9	r0049	1	0.5–6.0	bcc to fcc, melting (*V* sat.)	0.2; 10.0
	10	r0052	2	1.8–11.6	bcc to fcc, melting (*V* sat.)	0.2; 1.1
	10	r0055	1.5	2.2–9.0	bcc to fcc, melting (*V* sat.)	0.2; 1.8
Hibef_04	40	r0028	2.5	2.1–18.2	hcp to fcc, melting (*V* sat.)	0.2; 1.8
	43	r0031	4	3.2–21.7	hcp to fcc, melting (*V* sat.)	0.2; 1.1
	46	r0034	6	5.8–31.9	hcp to fcc, melting (*V* sat.)	0.2; 0.8
Hibef_60	50	r0587	2.8	1.2–17.1	fcc + hcp from start, melting (diff. scatt.)	39.7
	55	r0588	3.5	2.8–17.1	hcp to fcc, melting (diff. scatt.)	6.4; 38.2
	56	r0590	4.5	2.0–22.8	hcp + fcc from start, melting (no peak)	67.3
P1	80	r0417	0.1		X-ray transmission test	
	80	r0419	1	1.5–5.5	X-ray transmission test	
	76	r0422	2.5	0.9–15.7	X-ray transmission test	
	66	r0423	3	2.6–18.8	fcc + hcp from start, melting (no peak)	74.4
	69	r0435	4.5	3.9–27.6	fcc + hcp from start, melting (no peak)	31.1
Oxek_011	67	r0076	2	3.2–12.0	hcp to fcc, melting (diff. scatt.)	1.1; 8.2
	68	r0079	2.5	3.8–12.8	hcp to fcc, melting (diff. scatt.)	0.7; 9.8
Betsa_A	138	r0452	7	4.4–49.2	melting (diff. scatt.) + fcc	46.40
	139	r0467	12	5.1–73.0	melting (diff. scatt.) + fcc	15.8

(Fig. 4). The only exception is for cell Oxek_011 with a SiO_2 pressure medium, for which the 200_{fcc} reflection is consistently observed and isolated from other phases and, hence, used to determine the fcc-Fe individual grains volumes. The determination of the unit cell volume for ε-Fe requires at least two reflections. For this reason, we use both the 100 and 101 reflections; however, it is clear that those two diffraction spots originate from two different grains. Therefore, we associate the spots with minimum, median, and maximum 2θ positions for both 100 and 101 to evaluate maximum, median, and minimum unit cell volumes for hcp-Fe. In this process, volumes with unreasonable c/a values are ignored, i.e., if c/a falls outside the [1.55, 1.62] interval.[60] The overlap between the 111_{fcc} and 002_{hcp} reflections causes some of the diffraction spots identified as fcc to actually originate from the hcp phase, leading to unrealistically low values of volume for the fcc phase, as shown in Fig. 10(a).

This procedure allows us to obtain the distribution of unit cell volumes for the corresponding phase and its evolution throughout the heating cycle. The volume histograms are plotted against time to highlight thermal expansion and volume saturation that is used as a melt criterion.

An example illustrating the analysis procedure is presented in Fig. 10 for the run r0435 at 69 GPa where the measured fcc unit cell volume (a) and the number of detected diffraction spots (b) corresponding to the reflections 111_{fcc}, 100_{hcp}, and 101_{hcp} are reported as a function of time. Disregarding the unrealistically small unit cell volume, an outcome of the already mentioned confusion at low temperature between the 111_{fcc} and 002_{hcp} reflections, we can see that the fcc phase thermally expands during heating and saturates at a maximum $V = 38.075\,\text{Å}^3$.

Figure 10(b) shows that the number of fcc spots increases during the first 5 μs, while the number of hcp spots decreases, indicating the gradual transition from hcp to fcc. Peaks from the hcp phase disappear from the x-ray diffraction images after 25 μs of heating. Although several fcc grains are still observed after more than 35 μs, finite element modeling predicts the melting of the fcc phase at probing time after 15 μs of heating [Fig. 8(a)]. The sharp decrease in the number of fcc grains can, thus, be explained either by the melting of the bulk of the sample or by the recrystallization and unfavorable orientation of the fcc grains, or a combination of both processes.

E. Thermal pressure and *P*–*T* conditions

Most of the runs are at temperatures too low to acquire exploitable streak optical pyrometry (SOP) data. Moreover, the SOP signal is dominated by the hottest part of the sample averaged over several x-ray pulses and, thus, affected by several heating and cooling cycles of the sample. As shown in Figs. 8(a) and 9, this peak temperature can be several thousands of *K* greater than that of the sample during diffraction measurement and, thus, does not correspond to the phases observed in the diffraction patterns. Thus, in this paper, we do not use the SOP signal to evaluate the sample temperature.

The first pulse of a run probes the sample at ambient temperature, before the effect of x-ray heating (Fig. 2). As such, the starting pressure for each run is estimated using the sample's unit cell

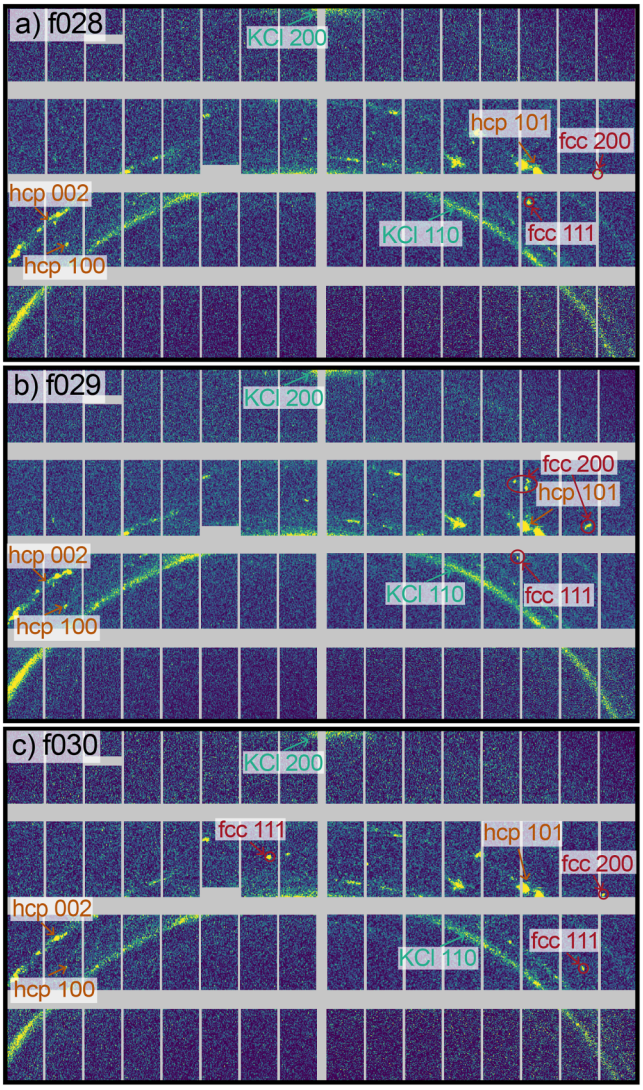

FIG. 7. Successive x-ray diffraction images extracted from run r0435 (4.5% tr) for cell P1. The pressure obtained from the analysis of the first frame of the run, when the sample is at 300 K, is 69 GPa. (a) Frame 28 at 5.98 μs. (b) Frame 29 at 6.20 μs. (c) Frame 30 at 6.42 μs. On all three frames, the diffraction figures of KCl and hcp-Fe do not change significantly. Conversely, the diffraction spots originating from the fcc phase appear and disappear in between frames, indicative of sample recrystallization.

volume deduced from the first image of the run and the Fe equation of state parameters from Ref. 61 for α-Fe and Ref. 62 for ε-Fe as well as for γ-Fe when this phase was detected in the quenched sample at ambient temperature. The starting pressure changes from run to run for the same sample on the same position (e.g., Appendix B, Fig. 15) and depends on the heating history of the sample at a given position.

The following pulses probe the sample during its cooling after x-ray heating (Fig. 2). We rely on equations of state of Fe and the distribution of unit cell volumes (e.g., Sec. III D) for the evaluation of temperature. At high temperatures, it is also necessary to account for thermal pressure P_{th}.[10,11,14,15,17,55,63,64]

Thermal pressure can vary between zero for the isobaric case, in which the sample container expands and accommodates the sample thermal expansion, and $dP_{th} = \int_{300\,\mathrm{K}}^{T} \alpha K_T \, dT$ for the isochoric model, where α and K_T are the thermal expansion coefficient and the isothermal bulk modulus, respectively, for the isochoric model. The reality lies between those two extreme cases, as shown using finite element modeling[14] or more recent x-ray diffraction experiments.[63] Indeed, the actual thermal pressure depends on numerous factors, such as the nature of the sample and PTM, the size of the diamond culets, gasket hole, etc. A factor x can, hence, be defined for scaling between the isobaric ($x = 0$) and isochoric ($x = 1$) models, with values of $x \geq 0.3$ often reported in the literature, depending on both the sample and the pressure medium.[10,14,15] This value of $x = 0.3$, however, has been evaluated in laser-heated diamond anvil cell experiments, but its applicability for use in x-ray heating experiments is yet to be assessed.

Here, we will assess values of x appropriate for x-ray heating experiments on runs fulfilling the criteria for melting. We used a previously determined melting curve (T_m^{HT} from Ref. 32) and assumed a known equation of state[62] and that the largest unit cell volume measured in runs reaching melting conditions corresponds to that of the *HT* solid phase just prior to melting. As already discussed, there are different families of melting curves for Fe published in the literature. T_m^{HT}, from Ref. 32, is used as a representative of the many studies (e.g., Refs. 17, 43, 65, and 66) supportive of a relatively high melting curve. T_m^{LT}, from Refs. 34 and 35 for the melting curves of γ-Fe and ε -Fe, respectively, is instead used as a representative of a second set of results supportive of a lower melting curve.

Figure 10(a) presents the evolution of the distribution of fcc unit cell volumes as a function of time in run r0435 starting from 69 GPa. These are compared to the expected volumes along the low temperature melting curve for $P = 69$ GPa for $x = 0$ (isobaric case, $V_{x=0}^{LT}$) and along the high-temperature melting curve for different values of x (isobaric and intermediate cases, V_x^{HT}). The maximum volume reached in solid fcc-Fe corresponds to the low temperature melting volume for $x = 0$. This would mean that for the T_m^{LT} curve to be in agreement with our experimental results, we need to completely disregard thermal pressure. Conversely, the maximum volume observed in solid is compatible with the *HT* melting curve when accounting for a thermal pressure between 10% and 20% of the isochoric pressure (best value $x = 0.16$).

The values of x determined for the different DAC loadings using T_m^{HT} are presented as a function of pressure in Fig. 11, and the corresponding P–T paths are presented in Fig. 1 together with the temperature obtained from the maximum volume with no thermal pressure ($x = 0$). For pressures above 100 GPa, we used the volume of the hcp phase to determine x. For both studied runs, we calculated the volume using two methods, either by considering both the 100_{hcp} and 101_{hcp} reflections (purple filled symbols in Figs. 1 and 11) or by considering solely the 100_{hcp} reflection and $c/a = 1.598$ (purple empty symbols in Figs. 1 and 11). The largest unit cell volumes determine a temperature that is higher than T_m^{LT}

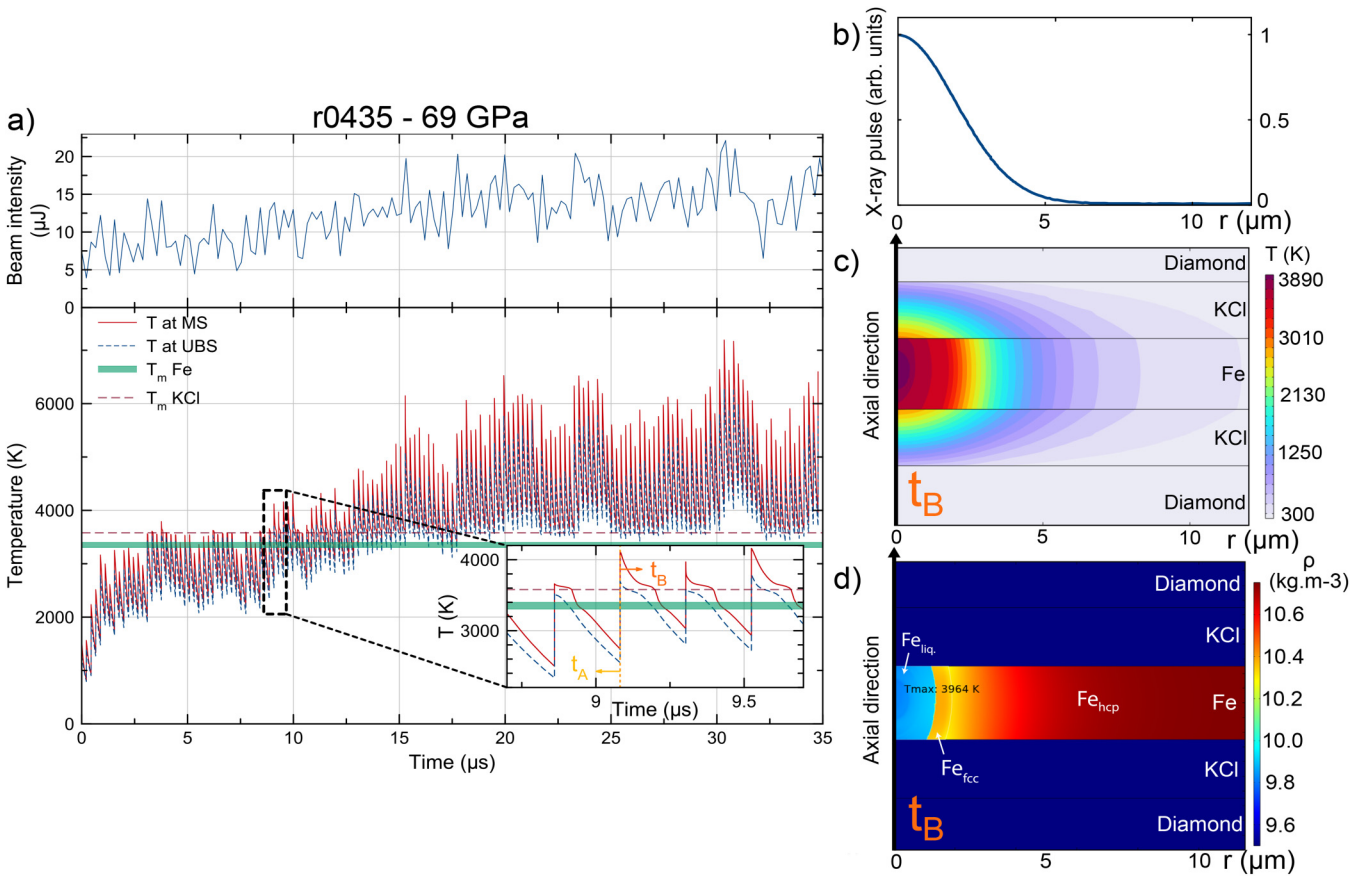

FIG. 8. Example of finite element modeling for run r0435 in the P1 cell for starting pressure $P_{300\,K} = 69$ GPa. The Fe foil and KCl layers have a thickness of 2.5 and 2 μm, respectively, and have been evaluated from electron microscopy analysis of the *postmortem* sample (see Ref. 57). (a) Temperature along the x-ray beam axis at $r = 0$ and the incident x-ray beam intensity as a function of time. MS, solid red line—temperature in the middle of the sample; UBS, dashed blue line—temperature of the upper sample boundary, i.e., at its interface with KCl. Melting temperatures T_m for Fe[32] and KCl[58] are shown as a green solid line and a dashed maroon line, respectively. The inset shows a zoom around pulse 42 at 9.08 μs. Instant t_A is the time just prior to the x-ray pulse and instant t_B the time just after its arrival. The peak temperature (at t_B) is above the melting curve, but the sample cools below T_m before the next diffraction is taken. (b) X-ray pulse intensity in an arbitrary unit as a function of r. (c) Temperature map at instant t_B in the sample, KCl, and part of the diamonds. Temperature at the center is high enough to melt Fe. (d) Density map at t_B in the sample, KCl, and part of the diamonds. The simulation predicts the sample to be molten at its core (i.e., $r = 0$) with a hot fcc ring and the colder hcp on the edge. The densities of the diamonds and KCl are outside of the presented colorscale, which was chosen to enhance the contrasts between the different phases inside the sample.

even when no thermal pressure is included, which is further supportive of the high-temperature melting curve.

By employing this protocol and thanks to the here-evaluated thermal pressure, temperature can then be deduced at any time from the measured unit cell volumes, the starting pressure at 300 K, deduced from the powder diffraction of the first frame of the run, and the x thermal pressure factor found for the DAC loading (see Figs. 12 and 13).

IV. RESULTS AND DISCUSSION

A. Effect of x-ray transmission

Figure 4 shows time series of integrated diffraction patterns for four different runs on cell P1, at pressures of 75 ± 9 GPa: run r0417 with 0.1% tr, run r0419 with 1% tr (1.5–5.4 μJ/pulse), run r0422 with 2.5% tr (0.9–15.7 μJ/pulse), and run r0435 with 4.5% tr (3.9–27.6 μJ/pulse).

With 0.1% x-ray transmission, the sample is probed with no evidence of easily observable residual heating at probe time. As transmission increases, so does sample heating. 2.5% x-ray transmission is sufficient to trigger the transformation from ε- to γ-Fe and even melt part of the sample. Finally, 4.5% tr allows us to fully transform the hcp into fcc in less than 20 μs, and the first sign of melting [decrease in fcc spots number, see Fig. 10(b)] appears before 15 μs.

Overall, for the DAC loadings presented here, the x-ray fluence required to induce phase transition increases with pressure. Indeed, the required x-ray transmission to form fcc-Fe ranges from

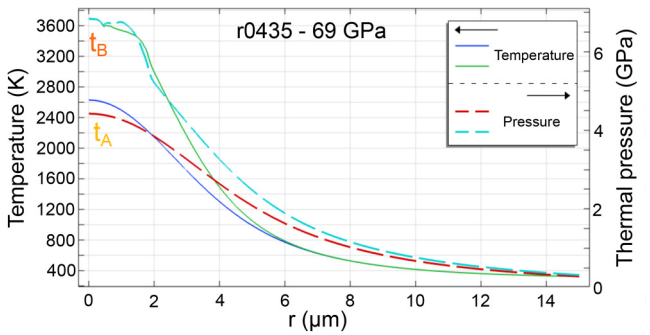

FIG. 9. Finite element modeled temperature and thermal pressure profile as a function of radial distance r at the upper sample—PTM boundary just before (t_A) and just after (t_B) an x-ray pulse at 9.08 μs for run r0435 in the P1 cell at starting $P_{300\,K} = 69$ GPa. The blue (red) and green (cyan) solid (dashed) lines correspond to the temperature (pressure) profile at times t_A and t_B, respectively.

0.2% tr at 10 GPa to 2.5% tr at 75 GPa while that required to melt the sample ranges from 0.5% tr at 10 GPa up to 7% tr at 135 GPa.

In addition to the x-ray transmission, the train envelope can be modified and tracked with the energy monitors. An example of such a pulse to pulse energy measurement is presented for r0435 of cell P1 at the top of Fig. 8(a). Measurements of pulse energies for all runs in this experiment are available as specified in the Data Availability statement.

B. Validation of phase identification

Below 100 GPa, the phases observed in the diffraction patterns correspond to the expected phase diagram, with a transition from bcc to fcc below 10 GPa (Fig. 6), and hcp to fcc to melt above 10 GPa (Fig. 4).

According to the literature (Ref. 31 and references therein), the α–γ–ε triple point is at 9.2 $\pm$ 1.3 GPa and 730 $\pm$ 50 K. During run r0037 of cell Hibef_22 at a starting pressure of 10 GPa, the co-existence of the three phases was observed, as shown in Fig. 5. After extracting the unit cell volumes of all three phases, the ranges of temperatures in each phase were calculated taking into account thermal pressure, as presented in Fig. 12(a). We find that the three phases co-exist up to 775 K. The α–γ–ε triple point is, hence, observed in the correct P–T range. hcp-Fe is never observed above 775 K, in agreement with known phase boundaries. This approach did not allow for the determination of phase transition temperatures for solid–solid transitions induced by heating, (*i.e.*, bcc to hcp

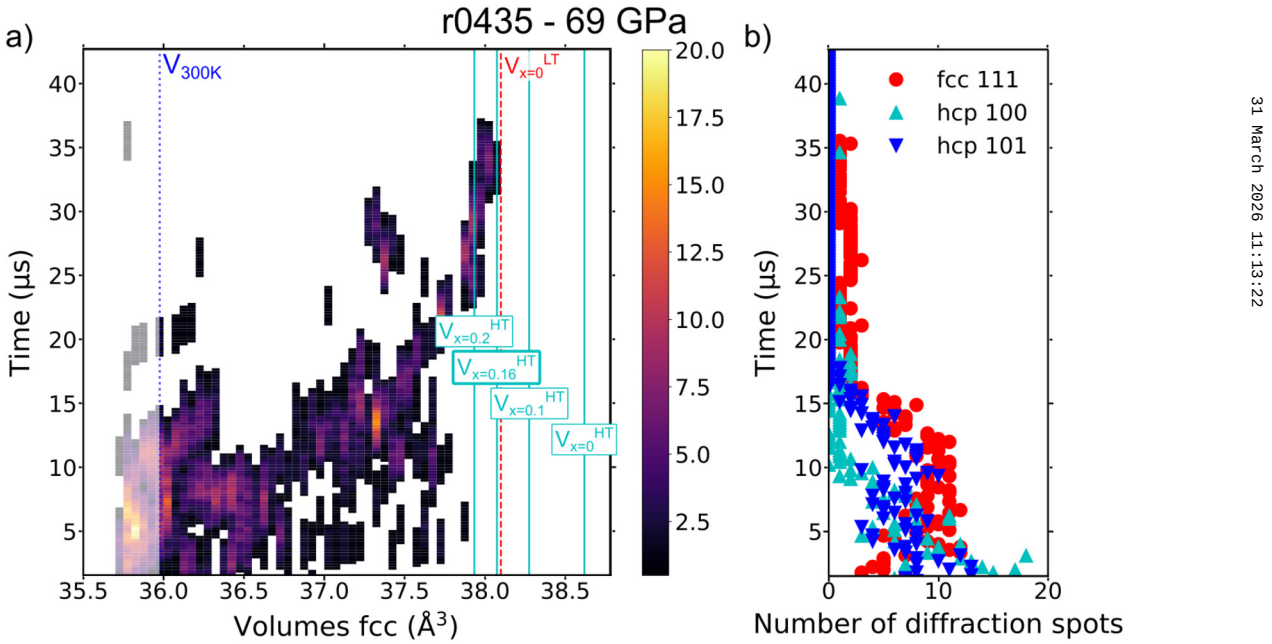

FIG. 10. Analysis of run r0435 on cell P1 with $P_{300\,K} = 69$ GPa [4.5% tr, Fig. 4(d)]. (a) Time-dependence of the histogram of fcc unit cell volumes deduced from individual spots detected in the 2θ range [20.2°; 20.8°]. Plotted as vertical bars are the unit cell volume of fcc-Fe quenched at 300 K from a previous run ($V_{300\,K}$, blue dotted line, corresponding to the isochoric unit cell volume at melting, $x = 1$) and the unit cell volume of fcc-Fe at melt assuming isobaric heating and the melting curves T_m^{HT} ($V_{x=0}^{HT}$, cyan line, Ref. 32) and T_m^{LT} ($V_{x=0}^{LT}$, red dashed line, Ref. 34). The highest measured unit cell volumes match $V_{x=0}^{LT}$, thus potentially compatible with solid fcc Fe at melting temperature, if the low melting temperature is assumed, but without any thermal pressure. If, instead, it is assumed that the grains showing the largest volume are at a temperature corresponding to the high melting curve, one deduces that thermal pressure is properly calculated with $x = 0.16$, $V_{x=0.16}^{HT}$ (see Sec. III E for details). Note that low values of fcc-Fe unit cell volumes (shaded area) are due to a confusion between the 002_{hcp} and 111_{fcc} peaks, which coincide at low temperature. (b) Number of detected diffraction spots as a function of time. Incidence of both 100_{hcp} (cyan up triangles) and 101_{hcp} (blue down triangles) spot follows a similar evolution, decreasing with time before disappearing after 10 and 16 μs, respectively. Conversely, 111_{fcc} (red circles) number of spot increases and reaches a maximum after 5 μs before decreasing again at 12 μs. All Fe diffraction peaks have disappeared before 40 μs.

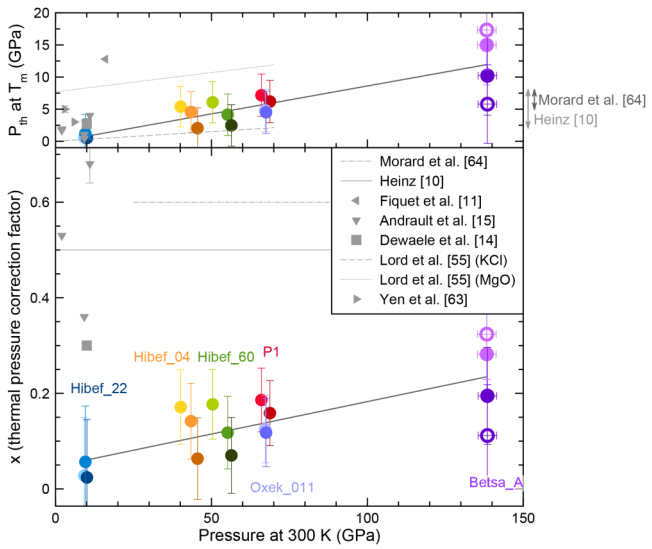

FIG. 11. Thermal pressure at melting temperature (top) and thermal pressure correction factor x (bottom) as a function of starting pressure. The names of the DACs are indicated. The colored circles are results from this study. The darker the color of the marker, the higher the x-ray transmission. For the Betsa_A cell, the empty symbols correspond to the calculations with a unit cell volume calculated from the 100_{hcp} only (c/a ratio imposed at 1.598), whereas the solid symbols are unit cell volume calculated from the 100 and 101 reflections on the two same runs. The thick lines are guides for the eyes. Data from the literature for different materials[10,11,14,15,55,63,64] are plotted in light gray. Raw data for this figure can be found in the link provided in the Data Availability section.

or hcp to fcc or bcc to fcc) as all the high-temperature solid phases can be quenched and observed at temperatures below their equilibrium stability field.

Cells Hibef_04, Hibef_60, Oxek_011, and P1, at pressures between 40 and 70 GPa, exhibit behavior similar to that presented in Fig. 4, that is, gradual heating with increasing x-ray transmission leading to the expected phase sequence: hcp-Fe to hcp and fcc-Fe mixture to pure fcc-Fe. As discussed above, detection of melting is more difficult as diffuse scattering can be hard to detect in the x-ray diffraction images (see Appendix C, Fig. 17), even after a full disappearance of all solid diffraction peaks.

Hence, repetitive x-ray pulse heating in DAC experiments is useful to detect temperature-induced phase transitions, the highest potential temperature in a given phase below a phase boundary. However, minimum temperatures to induce a phase transition while decreasing temperature are more difficult to evaluate due to the possibility to quench a high-temperature phase during the multiples cycles of fast heating and cooling.

Above 100 GPa (cell Betsa_A), hcp clearly dominates the diffraction pattern with some transient phenomena whose study is beyond the scope of this paper (Appendix F and Ref. 27).

No peak corresponding to a new phase caused by chemical contamination from the anvil was observed in the diffraction patterns.

C. Temperature gradients and time-evolution

Finite element models highlight how a wide range of P–T conditions are present within the volume probed by the x-ray beam [see Figs. 8(c) and 9]. These gradients can be observed directly in

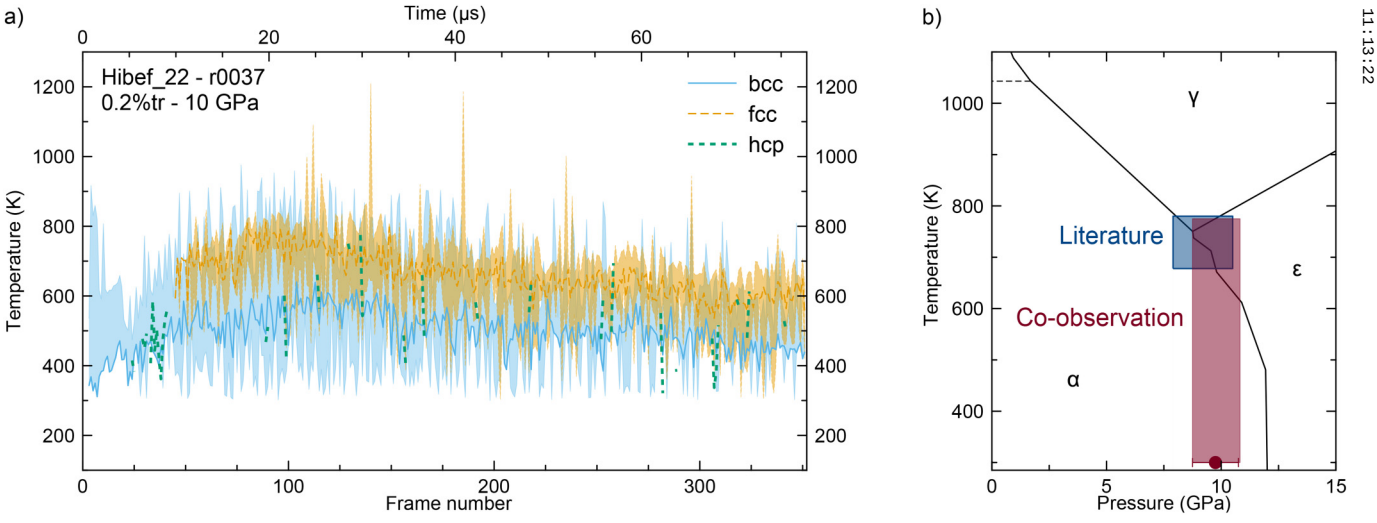

FIG. 12. (a) Temperature gradients as a function of frame number and time for run r0037 of cell Hibef_22 at a starting pressure of 10 GPa at 300 K and for $x = 0.036$. Solid lines correspond to the temperature determined from the median unit cell volume of bcc-Fe (blue), fcc-Fe (orange), and hcp-Fe (green). In addition, light blue and orange colors show the corresponding temperature gradients determined from the distribution of individual peak positions. (b) Phase diagram of Fe at the α–γ–ε triple point. Phase boundaries are from Ref. 31. The literature places the bcc–fcc–hcp triple point at 9.2 ± 1.3 GPa and 730 ± 50 K (blue rectangle). In our experiment, the three phases co-exist at $P = 10 \pm 1$ GPa and $T = 775$ K. Note that both fcc and hcp are quenchable to 300 K at this pressure and are co-observed with bcc as shown in the figure (red rectangle). The red point corresponds to the starting P with its uncertainty.

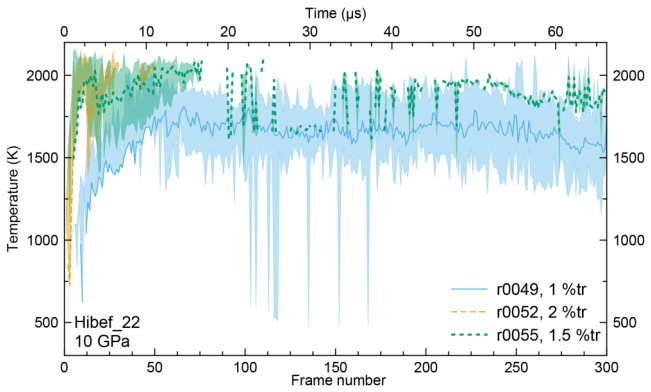

FIG. 13. Temperature gradients in the fcc-Fe as a function of frame number and time for runs r0049 (blue, 1%tr), r0052 (orange, 2% tr), and r0055 (green, 1.5% tr) of cell Hibef_22 at a starting pressure of 10 ± 1 GPa at 300 K. Solid lines correspond to the temperature determined from the median diffraction angle of fcc-Fe peaks. In addition, light blue, orange, and green colors highlight the corresponding temperature gradients determined from the distribution of individual spot positions. At higher temperatures, grains tend to grow, the number of grains reduces, and, hence, the apparent temperature gradients in fcc-Fe become negligible. The observed oscillations of the temperature deduced from the unit cell volume indicate solid fcc-Fe recrystallization between pulses.

diffraction images, which show evidence of grains with a range of lattice parameters due to different degrees of thermal expansion.

Indeed, Figs. 4 and 7 show grains co-existing under multiple conditions. Due to the nature of the x-ray heating experiment, grains laterally further away from the probed heating area, i.e., at nearly ambient temperature, may contribute to diffraction, along with the center portion of the sample, which can be at thousands of degrees and even molten (Fig. 9). Those gradients are mostly radial, with smaller axial gradients predicted by finite element modeling (Fig. 8).

For instance, as illustrated in Figs. 8 and 9, the sample at ~69 GPa and 9.08 μs is at a temperature ranging from room temperature to 2740 K when probed by the x-ray pulse. Simulations predict that, right after x-ray diffraction, the sample is volumetrically heated, leading to a maximum temperature of 4100 K at its center, 3600 K at the upper sample-PTM boundary, and a sample edge remaining at 300 K. When the next pulse arrives at 9.30 μs, the center of the sample is at 3070 K, the upper sample boundary at 2810 K, and the sample edge still at 300 K. When diffraction is collected with the pulse at 9.30 μs, the maximum temperature has, hence, dropped by 1030 K compared to the peak temperature reached 221.5 ns earlier.

Temperature gradients detected by x-ray diffraction depend on the x-ray transmission. Figure 13 shows the temperature evolution for three runs of the same DAC loading with three different x-ray transmissions. Looking at the temperature evolution of run r0049 (blue, lowest transmission), we can see that the temperature gradient is stable throughout the heating and consistent with expectations from the finite element calculations. For run r0055, at intermediate transmission, the apparent temperature gradient in the solid phase decreases quickly with barely any grains detected after 17.5 μs, and the rest of the sample probably molten. The same observation is also true at higher transmission, albeit on a faster timescale.

Co-existing phases in the diffraction patterns are, thus, (i) not necessarily under the same conditions, and (ii) cooling from a peak temperature reached 221.5 ns earlier, which can be over 1000 K higher (this drop in temperature increases directly with the peak temperature). For this reason, it is difficult to assess the location of a phase boundary based on our measurements. We, thus, find that the most efficient procedure to establish a phase diagram here is to track the highest temperature at which a solid grain is observed, assuming that this temperature will correspond to the uppermost location of the phase stability.

D. Thermal pressure

The estimation of thermal pressure is necessary to evaluate pressure and temperature based on x-ray diffraction. In DAC experiments, thermal pressure lies between the isobaric ($x = 0$) and isochoric ($x = 1$) boundary conditions. The determination of the thermal pressure correction factor, x, is a long standing issue in high pressure experiments. Values of 0.3 or more are often used in the literature depending on studies and materials.[10,14,15,64]

Here, we use a known melting curve for Fe and our measurements to evaluate the value of x for x-ray heating experiments (Fig. 11, color symbols). We find that x increases with pressure, ranging from 0.04 at 10 GPa to 0.23 at 130 GPa. For cells below 100 GPa, the scatter between values of x found for different runs of the same cell or for different cells at comparable pressures is similar. For the cell above 100 GPa, the differences between the different values of x arise from the difficulty to determine the maximum unit cell volume observed in the hcp phase. The increase of x with pressure is expected as both the sample and the PTM become stiffer (positive derivative of K_T with P). Stiffer materials will lead to more thermal pressure than softer materials.[14,55] However, we observe no difference between data collected with a SiO_2 or KCl PTM. Moreover, higher pressure means smaller experimental chamber and thinner PTM layers between the sample and the diamonds, which prevent thermal expansion as the anvils will not move.

The thermal pressure correction factor x reflects the capability of the PTM to accommodate for the sample expansion and, thus, may depend on the thermal history of the relaxation state of the PTM at the investigated position.[10,67] However, no systematic trend was found between the runs that were performed on an unrelaxed position (first significant heating) or on a position that had already gone through several significant heatings, where one might expect an annealed PTM and, hence, lower thermal pressure.

Intuitively, the thermal pressure may be expected to increase at higher heating rates. However, the opposite was observed in our experiments: x decreases with increasing x-ray beam transmission, which governs the heating rate. With a higher transmission, PTM reaches a higher peak temperature, high enough to melt it early in the run. A liquid PTM would better accommodate the thermal expansion of the sample, thus reducing the value of x.

Figure 11 shows the thermal pressure at melting as a function of the starting pressure at 300 K. It increases from $P_{th} = 0.8$ GPa

for $P_{300\,K} = 10$ GPa and 2140 K to $P_{th} = 12.1$ GPa for $P_{300\,K} = 138$ GPa and 4370 K. The values we obtain are consistent with finite element modeling. Indeed, for run r0435 of cell P1 at $P_{300\,K} = 69$ GPa, the simulated thermal pressure around T_m at instant t_B is 6.5 GPa, in agreement with the 6.2 GPa we find for the same run at melting conditions.

Literature values of x range between 0.3 and 0.7, based on continuum calculations,[10] finite element modeling,[14] comparison between DAC and large volume press experiments,[11,15] pressure changes during laser-heating,[55] or direct measurement of the pressure and temperature distribution during heatings.[63] Differences in thermal pressure estimates could be explained by the use of different samples/PTM combinations in addition to the different heating method. In addition, we note that our approach relies on a multi-crystal-like analysis, looking for the grain at the highest temperature rather than a mean sample temperature, as usually done in the standard powder diffraction analysis. Determining the values x by forcing the mean sample temperature to correspond to that of the melting curve would automatically increase the deduced values for x. This approach, however, would neglect the effect of temperature gradients that we know to be important. Finally, we note that the values of thermal pressure we obtain are in line with the results of finite element calculations for this sample configuration, which supports our experiment-based conclusions.

E. Iron melting temperature

Our data show grains with volumes inconsistent with the lower melting curve for iron published in the literature (Refs. 34 and 35) and are, hence, supporting the higher melting curve family for Fe at high pressure (Refs. 17, 32, 43, 65, and 66). Questions could be raised whether equilibrium has been reached, which has been a longstanding debate between the shock and static communities (e.g., Refs. 3, 32, 34, 35, 66, and 68–70).

While individual heating events are of short duration (fs) here, there are 222 ns between each heating and the subsequent probe. During these 222 ns, the sample cools by up to thousands of K (Fig. 8). FEM modeling indicates that there is sufficient time for the sample to crystallize from the liquid state. These experimental timescales are significantly longer than those of shock wave techniques, which, in addition, probe the sample upon heating rather than cooling. As such, one could argue that our measurements are at equilibrium since they probe the Fe sample returning from the molten state, with sufficient time to crystallize. Nevertheless, our measurements also show transient states in the solid portion of the phase diagram, which remain to be understood (Appendix F) and will be investigated later.

V. CONCLUSION

This study shows the feasibility of volumetrically heating a compressed iron sample up to megabar pressures using intense x-ray pulses delivered by a XFEL source. By tuning the x-ray intensity, we can explore different regions of the phase diagram, including solid–solid phase transition, and partially or totally molten samples. The known iron phase diagram has been reproduced, including the location of the bcc–fcc–hcp triple point at ≈9 GPa and ≈730 K, the hcp to fcc transition induced by temperature above 15 GPa, and the melting curve of Fe up to 150 GPa. In particular, the measured volumes and the known melting curve have been exploited to develop a dedicated metrology for x-ray heating experiments, accounting for thermal pressure.

Importantly, due to the rapid heating (∼25 fs) and subsequent quenching (∼222 ns) of the sample and short experimental time (<78 μs), chemical diffusion is very limited if not absent. As direct consequence, no chemical contamination of the Fe sample by the carbon from the anvils was observed in the diffraction data, unlike in pulsed laser-heating DAC experiments. Note, however, that a full study of carbon contamination of Fe samples in DAC experiments would require additional spectroscopy analyses,[22] which were not done here. The contamination risk can be further reduced by decreasing the number of x-ray pulses. Indeed, depending on the x-ray intensity and pressure of the sample, the molten state can be reached within a few pulses, and the solid signal can disappear quickly afterward. As such, not every measurements require the maximum 352 consecutive pulses we used here.

Thanks to the single-spot tracking analysis, temperature gradients can be accounted for and characterized. This technique also allows us to determine quantitative values for thermal pressure, which is essential to establish the P–T conditions at which the sample is probed. The thermal pressure values we obtain are lower than in most of the literature and strongly depend on the starting pressure, increasing from 0.8 GPa when heating to 2140 K at 10 GPa ($x = 0.036$) to 12.1 GPa when heating to 4370 K starting from 138 GPa ($x = 0.228$).

The exact P–T path induced by x-ray heating, however, can be difficult to establish. Currently, temperatures below ≈3000 K are difficult to measure using the SOP setup at the HED instrument. In addition, SOP measures the sample surface temperature, which may be up to 1000 K lower than that of the bulk sample, and is averaged over a duration during which the sample temperature can vary significantly. As for *in situ* x-ray diffraction, the sample is probed 221.5 ns after the peak temperature, during which the sample cooled by up to 1000 K or more. For the reasons listed above, locating phase boundaries in a phase diagram can be complicated, in particular, when high-temperature phases are quenchable. We find that the most reliable technique is to identify the highest temperature of existence of a given phase.

X-ray heating differs from the usual laser-heating of metallic samples by the way it heats the sample.[5,8] Indeed, x rays are absorbed by the core electrons that heat before equilibrating with the ionic network.[24,71] This would mean that two temperatures co-exist in the sample during and just after heating: a lower temperature for the ionic network and a higher temperature for the electronic cloud, which should equilibrate within tens of picoseconds.[71] The way this heating mechanism affects the observed temperatures and crystalline phases should be further investigated in the future. Indeed, recent first-principles calculations for iron at megabar pressures suggest that it changes the iron phase diagram at high electronic temperatures.[72]

This method is now ready for further studies, which will focus on fine effects of x-ray heating on the iron phase diagram. X-ray heating with pulsed XFEL sources can also be applied to other materials. The method is efficient to reach high temperature in the sub-μs timescale and, as we show here, induce phase transitions in

agreement with other methods of observations. Because the entire sample thickness is exposed to the x-ray beam, x-ray heating has the benefit of low axial temperature gradients. There are limitations, however. First, significant lateral temperature gradients and fast moving microstructures from frame to frame can be challenging to account for, which can be partly addressed by single peak extractions rather than a simple powder XRD analysis. Thermal pressure, also, will depend on the strength and compressibility ratios between the sample and the pressure medium, which might lead to complicated determination of the exact P/T conditions. As such, studies on a material with a previously calibrated equation of state, albeit at lower P/T conditions, as we do here, would be recommended. The state of matter obtained during the successive cycles of fast heating and cooling with the repeated X-pulses can also be affected by kinetics and sample history. Hence, a precise determination of temperature of phase transitions, for instance, should be analyzed with caution. Nevertheless, x-ray heating with pulsed XFEL sources is a relevant method to study the state of matter in conditions that were simply not attainable with conventional laser-heating DAC experiments and at fast timescales, hence limiting the risk for reactions with either the diamonds or pressure medium surrounding the sample.

ACKNOWLEDGMENTS

The authors are indebted to the HIBEF user consortium for the provision of instrumentation and staff that enabled this experiment. We acknowledge European XFEL in Schenefeld, Germany, for provision of x-ray free-electron laser beamtime at Scientific Instrument HED (High Energy Density Science) and would like to thank the staff for their assistance. We acknowledge DESY (Hamburg, Germany), a member of the Helmholtz Association HGF, for the provision of experimental facilities. We also acknowledge DESY (Hamburg, Germany), a member of the Helmholtz Association, for providing access to the experimental facility PETRA III and beamline P02.2 for sample screening. The authors also wish to thank L. Ehm for providing resources and K. Glazyrin for its help with the methodology. D.A. and S.B. have received funding from the European Research Council (ERC) under the European Union's Horizon 2020 research and innovation programme (Grant Agreement No. 724690). H.M. and E.K. were supported by the European Union's Horizon 2020 research and innovation programme (ERC Grant No. 864877) and UKRI STFC Grant No. ST/V000527/1. R.S.M., B.M., and Z.Y. were supported by the ERC under the European Union's Horizon 2020 research and innovation Programme (Grant Agreement No. 101002868) and RCUK- EPSRC (Grant No. EP/P024513/1). S.M., J.C., and H.G. are funded by the European Union (ERC, HotCores, Grant No. 101054994). Views and opinions expressed are, however, those of the author(s) only and do not necessarily reflect those of the European Union or the the European Research Council. Neither the European Union nor the granting authority can be held responsible for them. K.A. and K.B. acknowledge financial support by the Deutsche Forschungsgemeinschaft (DFG, German Research Foundation) via project AP262/2-2 (Project No. 280637173). This work was supported by Grant Nos. EP/S022155/1, EP/R02927X/1, and EP/Z533671/1 from the UK Engineering and Physical Sciences Research Council (EPSRC), M.I.M., and J.D.M. J.D.M. is grateful to AWE for the award of CASE Studentship P030463429. O.B.B. acknowledges the support of the Scottish Doctoral Training Program in Condensed Matter Physics (CM-CDT). G.M. and N.J. were supported by ANR grant MinDIXI (No. ANR-22-CE49-0006) and Labex OSUG@2020 (Investissements d'avenir—ANR10 LABX56) and 15-IDEX-0002 Université Grenoble Alpes. A.P.D. was supported by the European XFEL R&D project S-278. M.S.A. and T.X. were supported by NASA–Solar-System-Workings program under Grant No. 80NSSC17K0765. A.F.G. and E.E. were supported by the U.S. National Science Foundation grant (No. EAR-2049127), (No. CHE 2302437), and Carnegie Science. Part of this work was performed under the auspices of the U.S. Department of Energy by Lawrence Livermore National Laboratory under Contract No. DE-AC52-07NA27344 (H.C.). V.P. was supported by the National Science Foundation-Earth Sciences (No. EAR-658 1634415).

AUTHOR DECLARATIONS

Conflict of Interest

The authors have no conflicts to disclose.

Author Contributions

Hélène Ginestet: Formal analysis (equal); Methodology (equal); Software (equal); Visualization (equal); Writing – original draft (equal); Writing – review & editing (equal). **Rachel J. Husband:** Conceptualization (equal); Investigation (equal); Software (equal). **Nicolas Jaisle:** Data curation (equal); Investigation (equal); Methodology (equal); Software (equal); Validation (equal); Visualization (equal); Writing – original draft (equal); Writing – review & editing (equal). **Eric Edmund:** Investigation (equal); Writing – review & editing (equal). **Zuzana Konôpková:** Conceptualization (equal); Data curation (equal); Investigation (equal); Methodology (equal); Project administration (equal); Resources (equal); Supervision (equal); Writing – review & editing (equal). **Cornelius Strohm:** Investigation (equal); Methodology (equal); Resources (equal); Supervision (equal). **Madden S. Anae:** Investigation (equal). **Daniele Antonangeli:** Funding acquisition (equal); Resources (equal); Writing – review & editing (equal). **Karen Appel:** Funding acquisition (equal); Investigation (equal); Methodology (equal); Resources (equal). **Orianna B. Ball:** Investigation (equal). **Marzena Baron:** Investigation (equal). **Silvia Boccato:** Investigation (equal); Writing – review & editing (equal). **Khachiwan Buakor:** Investigation (equal). **Julien Chantel:** Investigation (equal). **Hyunchae Cynn:** Conceptualization (equal); Investigation (equal). **Anand P. Dwivedi:** Investigation (equal); Writing – review & editing (equal). **Heinz Graafsma:** Investigation (equal); Resources (equal). **Egor Koemets:** Investigation (equal); Resources (equal). **Torsten Laurus:** Investigation (equal); Resources (equal). **Hauke Marquardt:** Conceptualization (equal); Funding acquisition (equal); Project administration (equal); Supervision (equal); Writing – review & editing (equal). **Bernhard Massani:** Investigation (equal). **James D. McHardy:** Conceptualization (equal); Investigation (equal); Methodology (equal); Writing – review & editing (equal). **Malcolm**

I. McMahon: Investigation (equal); Methodology (equal); Resources (equal). **Vitali Prakapenka:** Investigation (equal). **Jolanta Sztuk-Dambietz:** Data curation (equal). **Minxue Tang:** Investigation (equal). **Tianqi Xie:** Investigation (equal). **Zena Younes:** Investigation (equal); Writing – review & editing (equal). **Ulf Zastrau:** Conceptualization (equal); Methodology (equal); Resources (equal). **Alexander F. Goncharov:** Investigation (equal); Resources (equal). **Clemens Prescher:** Conceptualization (equal); Data curation (equal); Methodology (equal); Project administration (equal); Software (equal). **Agnès Dewaele:** Investigation (equal); Resources (equal); Writing – review & editing (equal). **R. Stewart McWilliams:** Conceptualization (equal); Funding acquisition (equal); Investigation (equal); Methodology (equal); Resources (equal); Supervision (equal). **Guillaume Morard:** Conceptualization (equal); Investigation (equal); Methodology (equal); Project administration (equal); Writing – review & editing (equal). **Sébastien Merkel:** Conceptualization (equal); Data curation (equal); Formal analysis (equal); Funding acquisition (equal); Investigation (equal); Methodology (equal); Project administration (equal); Resources (equal); Software (equal); Supervision (equal); Validation (equal); Visualization (equal); Writing – original draft (equal); Writing – review & editing (equal).

DATA AVAILABILITY

The original European XFEL data are located at https://in.xfel.eu/metadata/doi/10.22003/XFEL.EU-DATA-003063-00 and will be publicly available in 2025 after the embargo period of 3 years. Source data for figures and intermediate data processing results are provided in Zenodo at https://zenodo.org/records/17950889, Ref. 84.

APPENDIX A: ESTIMATING UNCERTAINTIES

The pressure at 300 K was calculated for the hcp phase using three different equations of state. Comparison between the different results is plotted in Fig. 14.

The main sources of uncertainty in our analysis arise from (i) the estimation of the sample unit cell volumes based on the XRD data, (ii) estimations of pressures using published equations of state, and (iii) the assumed melting temperature of iron at high pressure and temperature.

Uncertainties arising from different equations of state were accounted for when calculating sample pressures at ambient temperature. The uncertainty on pressure deduced from the hcp unit cell volume is estimated by comparing results from several equations of state (EoSs) found in the literature (Refs. 73 and 74, see Fig. 14). Estimating an uncertainty on pressure for the other phases (α and γ-Fe) is more difficult as less EoSs are available in the literature. Therefore, we arbitrarily set the uncertainty on pressure to 1 and 3 GPa below and above 100 GPa, respectively.

The uncertainty in determining the thermal pressure scaling value, x, comes from the uncertainties in the ambient pressure before heating, the volume of the unit cell of the hottest sample grains, and the melting temperature. Uncertainty on pressure is set as above. Based on the distribution of unit cell volumes measured in the sample, we assume an uncertainty of $\pm 0.025\,\text{Å}^3$ at melting. As for temperature, the issue arising from the disparities in the literature on the melting curve is addressed in Secs. III E and IV E. Since the largest volumes measured in a solid phase at several pressures exceed the volume expected at melting when a low melting temperature is assumed [T_m^{LT}, see Figs. 10(a) and 1], we only consider the upper-bound melting curve T_m^{HT} in our calculation of x, with an uncertainty of 200 K.

Additionally, looking at the variation of $P_{300\,\text{K}}$ between successive runs, we cannot be certain that the cold pressure of the sample when it reaches melting is the same as the one determined at the beginning of the run. This unpredictability of the evolution of the cold pressure during the run scatters the values of x we find. Indeed, if the cold pressure at melting is less than at the beginning of the heating, the measured temperature is underestimated and so is x. On the contrary, if the cold pressure has increased, the temperature is overestimated and so is x.

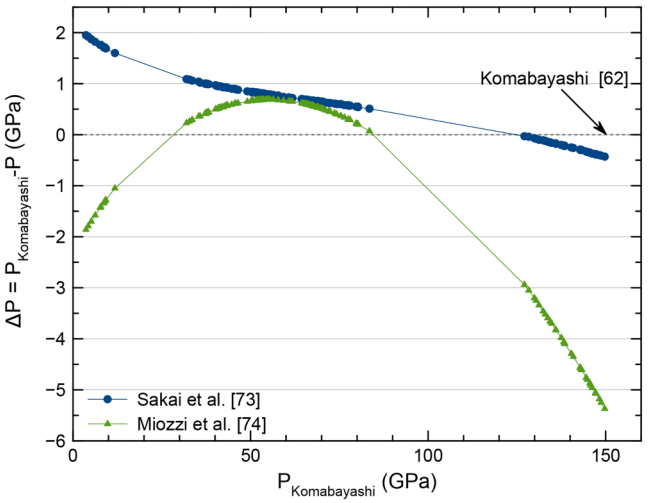

FIG. 14. Comparison between the different equations of state for hcp Fe. The pressures obtained with the equations of state from Refs. 73 and 74 are compared to that obtained with the equation of state from Ref. 62 for all the runs presented in this study using the hcp-Fe volume on the first frame.

APPENDIX B: PRESSURE CHANGES BETWEEN RUNS

Due to the pressure gradients that can develop in the DAC upon compression, pressure can change with position within the sample chamber. Moreover, on a same sample position, cycles of heating, cooling, and phase transformations can lead to relaxation of stress in both the pressure medium and the sample.[67] Examples of such variations of the pressure in the DAC are shown in Fig. 15.

The repeated cycles of x-ray heating induce relaxation of stress at the heated sample position, as shown for the first position in Hibef_04, or the second position in Betsa_A. The reduction of pressure, however, seems localized as other positions remain at higher pressure, as shown for the different positions in Hibef_04. Moreover, the relaxation of the PTM can sometimes be seen by the sharpening of its 110 diffraction peak after several cycles on a same position. In other cases, pressure of the PTM can increase at the

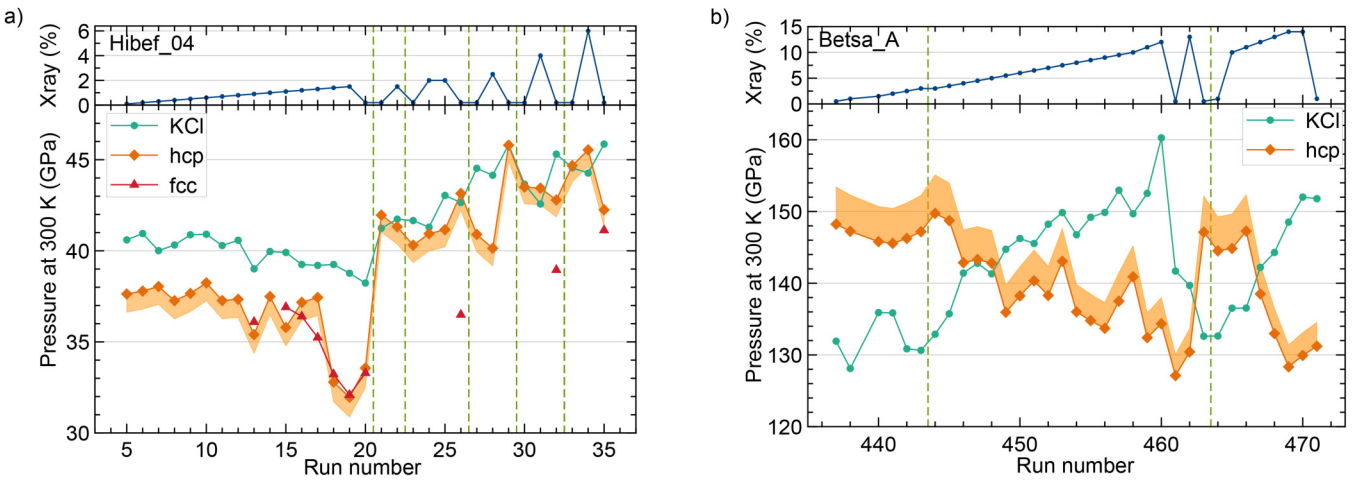

FIG. 15. X-ray transmission (top) and starting 300 K pressure (bottom) as a function of run number for cells Hibef_04 (a) and Betsa_A (b). These are deduced from the x-ray diffraction patterns collected with the first pulse in an x-ray train. The orange zone corresponds to the range of pressure calculated using different equations of state (see Appendix A). The dashed vertical green lines mark the times at which the sample was moved to a new position. The pressure depends on the heating history of the position.

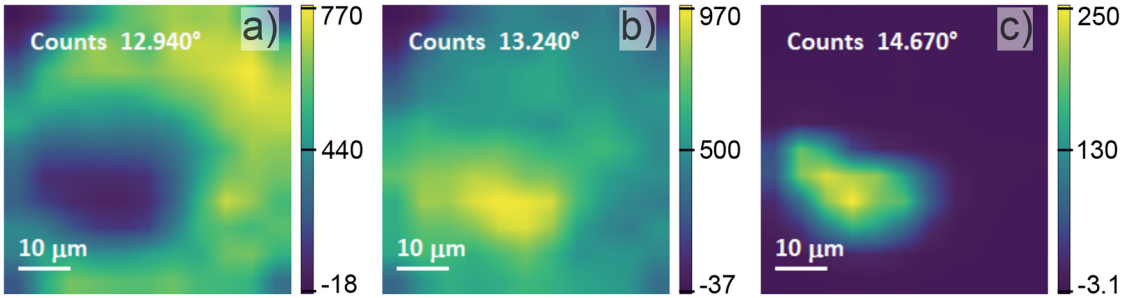

FIG. 16. X-ray diffraction mapping of sample P1 after the experiment taken at the Extreme Conditions Beamline P02.2 at PETRA III ($\lambda = 0.4839$ Å) with 5 μm steps using xdi software.[75] The color scale is proportional to the diffraction intensity (in arbitrary units). (a) Map of the lower 2θ part of the KCl 110 peak (low pressure). (b) Map of the larger 2θ part of the KCl 110 peak (high pressure). (c) Map of the fcc 111 peak (heated position). The increase of KCl pressure matches the position of the quenched fcc, which is that of the heated position.

heated point, as shown in Fig. 16. Note that pressures deduced from fcc-Fe at 300 K are not always consistent with those deduced from hcp-Fe and KCl, which is not surprising as fcc-Fe is a metastable phase under those conditions. We can also note that, depending on the DAC, the evolution of the pressure deduced from the PTM and the Fe can be similar (Hibef_40) or reversed (Betsa_A).

APPENDIX C: DIFFUSE SCATTERING

As shown in the examples in Fig. 17, the diffuse scattering signal is difficult to observe. This is due to the lack of pinhole and the intensity of the solid signal. We, hence, additionally relied on other criteria to determine melting (Table II).

APPENDIX D: FINITE ELEMENT MODELING ANALYSIS

The numerical model used to determine the temperature evolution induced by x-ray heating in run r0435 was built using the commercial COMSOL software. The geometry of the DAC and the contained assemblage was built assuming a two-dimensional axisymmetric geometry. Thickness of the sample was set to 2.5 μm, sandwiched between two 2 μm KCl layers and surrounded by a 6.5 μm thick KCl cylinder. The sample was assumed to have a cylindrical shape with radius $r = 40\,\mu$m and surrounding KCl hosting the cylinder with a radius of $r = 120\,\mu$m. Figure 18 highlights the main aspects of the geometry and the mesh used in the model. The heat equation was solved using quadratic discretization. Details about the way the volumetric x-ray heat source is absorbed can be found in Ref. 56. A 18 keV x-ray absorption coefficient was

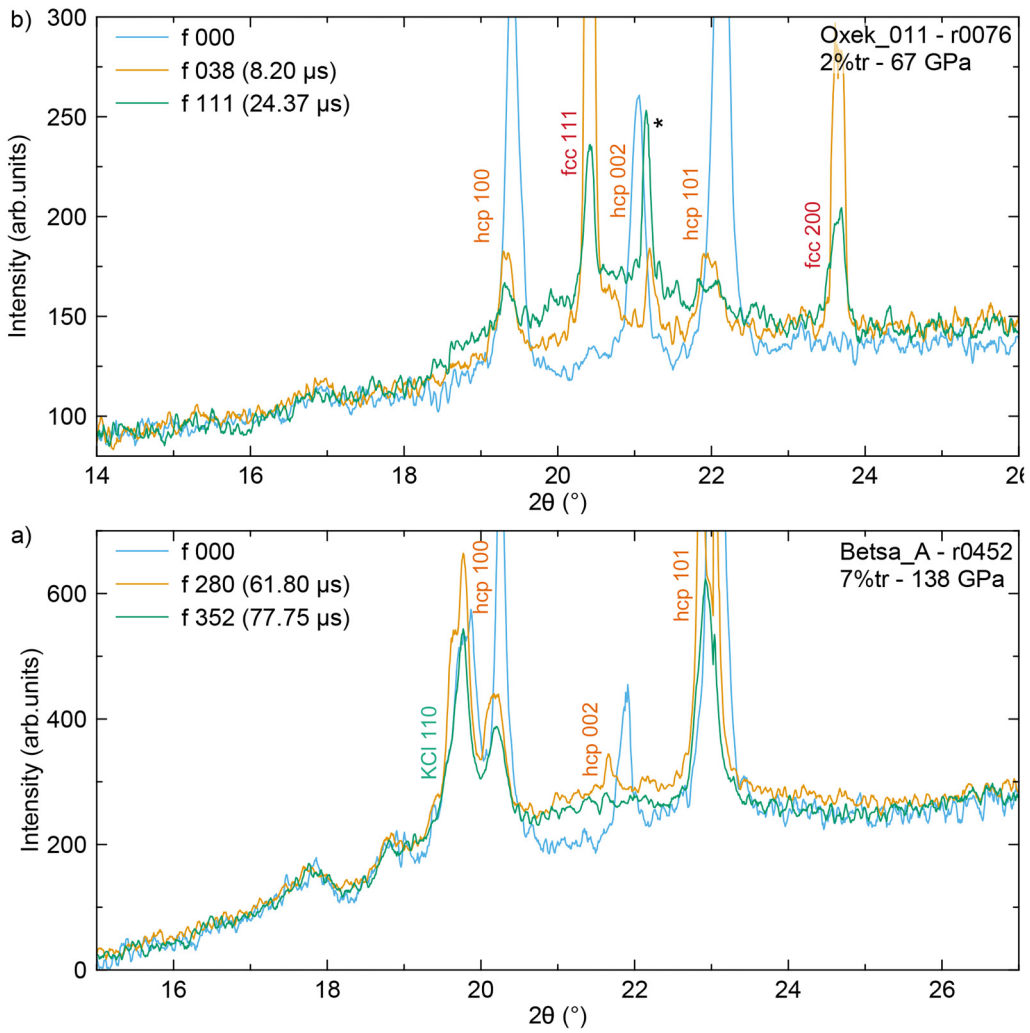

FIG. 17. Diffuse scattering from molten Fe. (a) Diffraction patterns of frames number 1, 280, and 352 of run r0452 from the Betsa_A cell with a starting pressure of 138 GPa. Patterns intensities were scaled based on background measured at low angle, where no diffraction is expected. The baseline for frames 280 and 352 shows an elevation with respect to the first frame in the ∼20° – 23° range, which can be attributed to weak diffuse scattering from molten Fe. The appearance of a weak diffuse scattering signal correlates with a decrease of the hcp peaks intensities and with a total disappearance of 002. (b) Diffraction patterns of frames number 1, 38, and 111 of run r0076 from the Oxek_011 cell with a starting pressure of 67 GPa. The peak labeled with a star is from the SiO_2 pressure medium, which heats and crystallizes during the run. The baselines for frames 38 and 111 show an elevation with respect to the first frame in the ∼20° – 23° range, which can be attributed to weak diffuse scattering from molten Fe.

disregarded for the gasket area owing to its great distance to the beam source. To account for solid mechanics, the solver used quadratic serendipity discretization and assumed quasi-static structural transient behavior.

The material properties (diamond, Re, Fe, KCl) used in the model are listed in Table III. When assumed necessary (i.e., supposed to have a non-negligible effect on temperature evolution), material property variations with pressure and temperature were included in the model. Such variations were included in the model by generating text files of properties (e.g., 10 000 densities calculated over 100 × 100 volumes and pressures over the valid publication range) that were then imported into COMSOL, which then achieves linear interpolation to infer the properties at the required pressure and temperature. Note that some values, such as iron thermal conductivity at extreme pressure and temperature, can still be controversial at some conditions as contradictory values have been published. Thermal stresses (i.e., pressure) induced through x-ray heating were included using the same procedure described in Ref. 56. Thermal expansion coefficients that induce thermal pressure

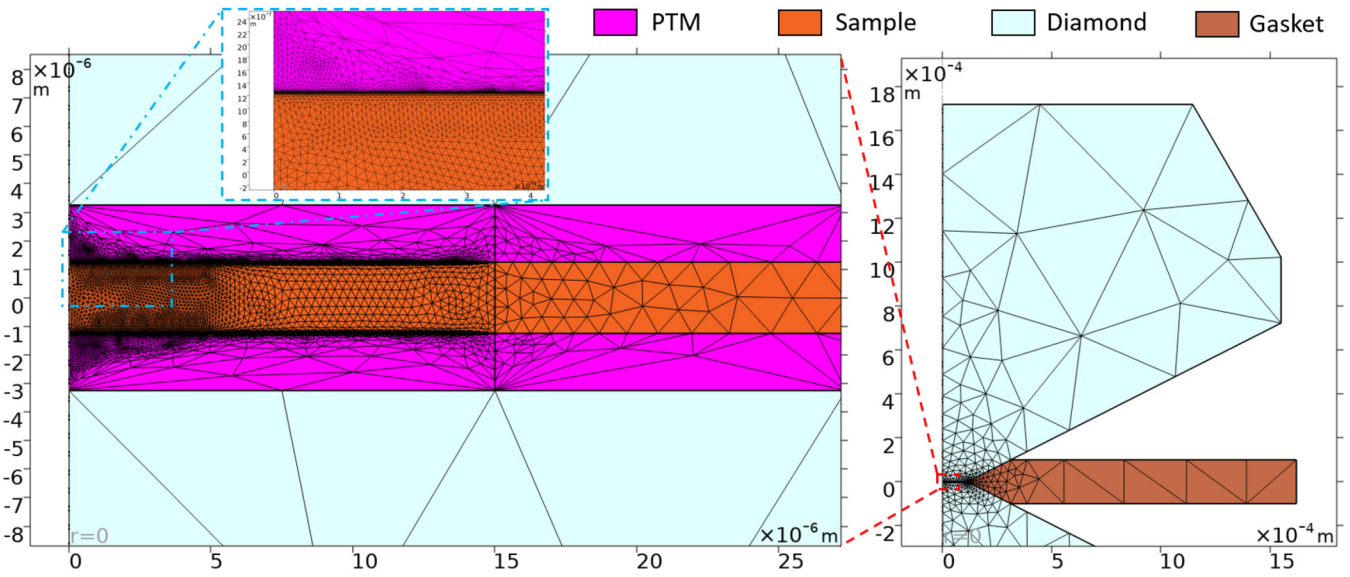

FIG. 18. DAC geometry and the corresponding mesh used for the simulation in the COMSOL model. Mesh has been refined at the locations where strong temperature and pressure gradients are expected, such as at the sample/PTM interface. To reduce computation time, the mesh element size has been increased where minimal variations are expected.

are listed in Table III. Shear modulus G was assumed to drop to zero upon melting.

The maps with the different phase extents in the sample [i.e., Fe-hcp, Fe-fcc, and liquid Fe, see Fig. 8(d)] were obtained by using the phase change and melting temperatures defined in the model. Whenever mentioned, the temperatures are either given for the upper border of the sample (UBS) or in the middle of the sample (MS), both located on the axis of symmetry. Including phase change allows us to account for latent heat in the temperature evolution as well for a smooth change in properties from one phase to another. Thermal conductivity of fcc iron at the considered conditions is poorly studied and was arbitrarily set to 100 W (m K)$^{-1}$. Melting of diamond and rhenium were not considered as they always remain close to ambient temperature. The thermal stress in the model was calculated the same way as described in Ref. 56 using the thermal expansion coefficients and bulk and shear moduli provided in Table III.

TABLE III. List of material properties used in the numerical model. [from top to bottom: density (ρ); heat capacity (C_P); thermal conductivity (k_{th}); melting temperature (T_m); parameters of the Simon–Glatzel equation, $T_0 \cdot (P/a + 1)^{(1/c)}$ (with P in GPa); absorption coefficient at 18 keV ($\mu_{X\text{-ray}}$); thermal expansion coefficient (α_L); shear modulus (G); and bulk modulus (K)]. The var. mention stands for the variable material property. All absorption coefficients were calculated from the official center for x-ray optics of the Berkeley lab website.[76]

Material	Diamond	Re	KCl	Fe_{hcp}, Fe_{fcc}, $Fe_{liq.}$
ρ (kg m^{-3})	3520	21 020	EoS[77]	EoS,[74] EoS,[78] EoS[79]
Cp [J (kg K)$^{-1}$]	var.	140	690	var.
k_{th} [W (m K)$^{-1}$]	990	48	12.5	var.,[80] 100, 40
T_{melt} (K) (T_0/a/c)	ø	ø	1323/2.2/2.7[58]	var.[a] (1811/23/2.26)[81]
$\mu_{X\text{-ray}}$(m^{-1})	158	ø	2513	26 316
α_L (K^{-1})	8×10^{-7}	6×10^{-6}	3.647×10^{-5}	10.6×10^{-6}
K (GPa)	446	332	17.2	160
G (GPa)	529.6	182	6.24	78 (fcc, hcp), 0

[a]Polynomial from Ref. 17: $(635 + 12.59\ P + 0.385\ P^2 - 0.0022\ P^3)$.

APPENDIX E: TEMPERATURE EVOLUTION FOR RUN R0435

An example of the evolution of the temperature deduced from the unit cell volumes is presented in Fig. 19 for run r0435 at a starting pressure of 69 GPa. We can observe the *HT* fcc phase being quenched far below its stability temperature domain. Moreover, the temperature from the hcp phase is sporadic due to the difficulty to assign two different reflections to a same grain to obtain realistic unit cell volumes.

APPENDIX F: DISORDER ABOVE 100 GPa

In DAC Betsa_A, different transient phenomena are visible, such as stacking faults or appearance of fcc grains. Those signs of disorder render the phase identification less straightforward, especially since fcc and hcp are structurally close and differ only by their stacking sequence.[82,83] Due to their fickle behavior, properly tracking and explaining such phenomena requires a different metrology and a dedicated study that goes beyond the scope of this paper.[27]

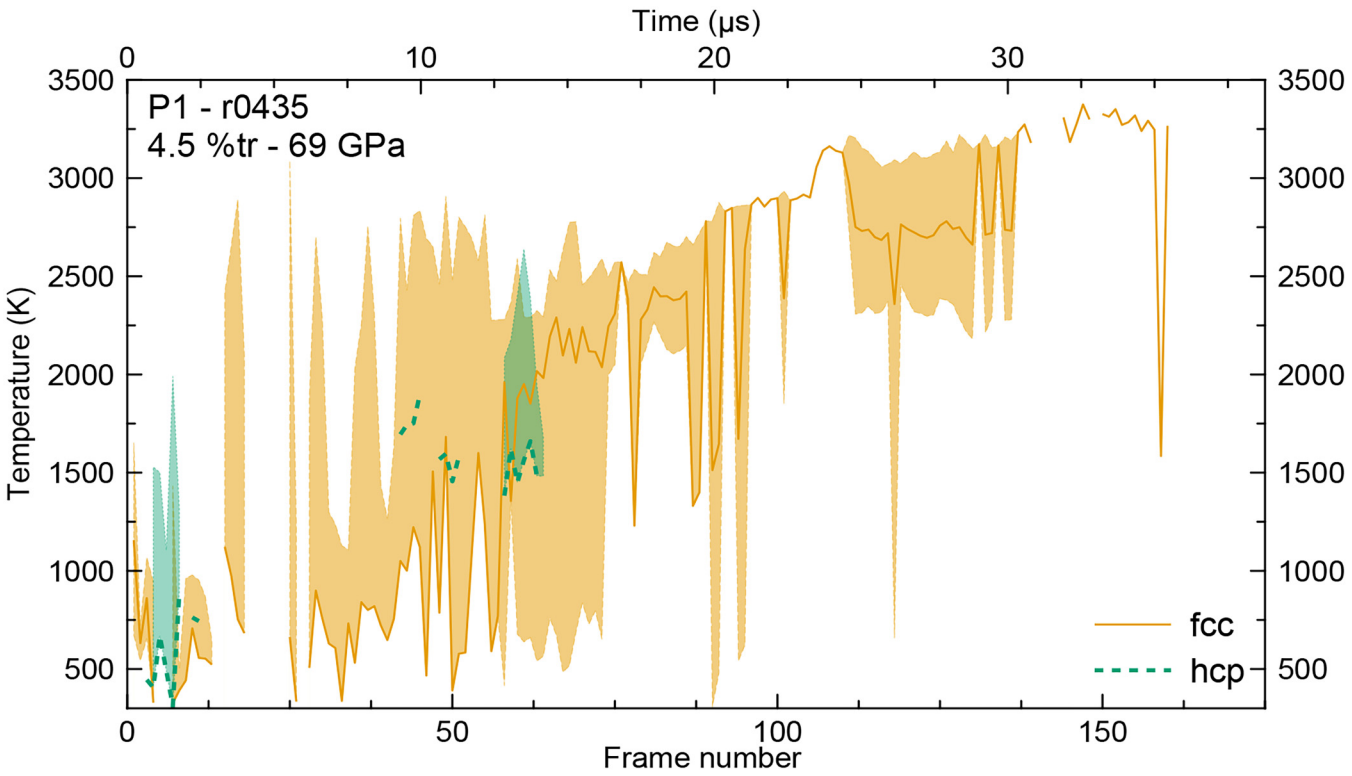

FIG. 19. Temperature as a function of frame number for r0435 of cell P1 at a starting pressure $P_{300\,K} = 69$ GPa. The median temperature of the fcc phase is plotted as an orange solid line. The orange area corresponds to the minimum and maximum temperatures for all fcc grains we identify. The blue dashed line is the temperature from the hcp phase. The blue area corresponds to the minimum and maximum temperatures for all hcp grains we identify. We can see that the gradient of temperature in the fcc phase decreases with time. Moreover, the maximum temperature reached in the hcp phase is below the known hcp to fcc transition temperature (2560 ± 175 K at 70 GPa[32,33]).

REFERENCES

[1]R. J. Hemley and N. W. Ashcroft, "The revealing role of pressure in the condensed matter sciences," Phys. Today **51**(8), 26–32 (1998).

[2]V. Cerantola, A. D. Rosa, Z. Konôpková, R. Torchio, E. Brambrink, A. Rack, U. Zastrau, and S. Pascarelli, "New frontiers in extreme conditions science at synchrotrons and free electron lasers," J. Phys.: Condens. Matter **33**, 274003 (2021).

[3]R. G. Kraus, R. J. Hemley, S. J. Ali, J. L. Belof, L. X. Benedict, J. Bernier, D. Braun, R. E. Cohen, G. W. Collins, F. Coppari, M. P. Desjarlais, D. Fratanduono, S. Hamel, A. Krygier, A. Lazicki, J. Mcnaney, M. Millot, P. C. Myint, M. G. Newman, J. R. Rygg, D. M. Sterbentz, S. T. Stewart, L. Stixrude, D. C. Swift, C. Wehrenberg, and J. H. Eggert, "Measuring the melting curve of iron at super-Earth core conditions," Science **375**, 202–205 (2022).

[4]*Ultrahigh-Pressure Mineralogy: Physics and Chemistry of the Earth's Deep Interior*, Reviews in Mineralogy No. 37, edited by R. J. Hemley (Mineralogical Society of America, Washington, DC, 1998).

[5]S. Anzellini and S. Boccato, "A practical review of the laser-heated diamond anvil cell for university laboratories and synchrotron applications," Crystals **10**, 459 (2020).

[6]J. A. Montoya and A. F. Goncharov, "Finite element calculations of the time dependent thermal fluxes in the laser-heated diamond anvil cell," J. Appl. Phys. **111**, 112617 (2012).

[7]S. Deemyad, E. Sterer, C. Barthel, S. Rekhi, J. Tempere, and I. F. Silvera, "Pulsed laser heating and temperature determination in a diamond anvil cell," Rev. Sci. Instrum. **76**, 125104 (2005).

[8]P. Parisiades, "A review of the melting curves of transition metals at high pressures using static compression techniques," Crystals **11**, 416 (2021).

[9]R. Sinmyo and K. Hirose, "The Soret diffusion in laser-heated diamond-anvil cell," Phys. Earth Planet. Inter. **180**, 172–178 (2010).

[10]D. L. Heinz, "Thermal pressure in the laser-heated diamond anvil cell," Geophys. Res. **17**, 1161–1164, https://doi.org/10.1029/GL017i008p01161 (1990).

[11]G. Fiquet, D. Andrault, J. Itié, P. Gillet, and P. Richet, "X-ray diffraction of periclase in a laser-heated diamond-anvil cell," Phys. Earth Planet. Inter. **95**, 1–17 (1996).

[12]L. Libon, G. Spiekermann, I. Blanchard, J. M. Kaa, S. Dominijanni, M. J. Sieber, M. Förster, C. Albers, W. Morgenroth, C. McCammon, A. Schreiber, V. Roddatis, K. Glazyrin, R. J. Husband, L. Hennet, K. Appel, and M. Wilke, "Reevaluating the fate of subducted magnesite in the Earth's lower mantle," Phys. Earth Planet. Inter. **355**, 107238 (2024).

[13]A. Ricolleau, Y. Fei, E. Cottrell, H. Watson, L. Deng, L. Zhang, G. Fiquet, A. Auzende, M. Roskosz, G. Morard, and V. Prakapenka, "Density profile of pyrolite under the lower mantle conditions," Geophys. Res. Lett. **36**, L06302, https://doi.org/10.1029/2008GL036759 (2009).

[14]A. Dewaele, G. Fiquet, and P. Gillet, "Temperature and pressure distribution in the laser-heated diamond–anvil cell," Rev. Sci. Instrum. **69**, 2421–2426 (1998).

[15]D. Andrault, G. Fiquet, J.-P. Itié, P. Richet, P. Gillet, D. Häusermann, and M. Hanfland, "Thermal pressure in the laser-heated diamond-anvil cell: An X-ray diffraction study," Eur. J. Mineral. **10**, 931–940 (1998).
[16]I. Uts, K. Glazyrin, and K. K. M. Lee, "Effect of laser annealing of pressure gradients in a diamond-anvil cell using common solid pressure media," Rev. Sci. Instrum. **84**, 103904 (2013).
[17]G. Morard, S. Boccato, A. D. Rosa, S. Anzellini, F. Miozzi, L. Henry, G. Garbarino, M. Mezouar, M. Harmand, F. Guyot, E. Boulard, I. Kantor, T. Irifune, and R. Torchio, "Solving controversies on the iron phase diagram under high pressure," Geophys. Res. Lett. **45**, 11074–11082, https://doi.org/10.1029/2018GL079950 (2018).
[18]V. Prakapenka, G. Shen, and L. Dubrovinsky, "Carbon transport in diamond anvil cells," High Temp.-High Press. **35/36**, 237–249 (2003).
[19]A. Dewaele, M. Mezouar, N. Guignot, and P. Loubeyre, "High melting points of tantalum in a laser-heated diamond anvil cell," Phys. Rev. Lett. **104**, 255701 (2010).
[20]G. Weck, V. Recoules, J.-A. Queyroux, F. Datchi, J. Bouchet, S. Ninet, G. Garbarino, M. Mezouar, and P. Loubeyre, "Determination of the melting curve of gold up to 110 GPa," Phys. Rev. B **101**, 014106 (2020).
[21]Z. M. Geballe and R. Jeanloz, "Origin of temperature plateaus in laser-heated diamond anvil cell experiments," J. Appl. Phys. **111**, 123518 (2012).
[22]G. Aprilis, I. Kantor, I. Kupenko, V. Cerantola, A. Pakhomova, I. E. Collings, R. Torchio, T. Fedotenko, S. Chariton, M. Bykov, E. Bykova, E. Koemets, D. M. Vasiukov, C. McCammon, L. Dubrovinsky, and N. Dubrovinskaia, "Comparative study of the influence of pulsed and continuous wave laser heating on the mobilization of carbon and its chemical reaction with iron in a diamond anvil cell," J. Appl. Phys. **125**, 095901 (2019).
[23]W. Decking, S. Abeghyan, P. Abramian, A. Abramsky, A. Aguirre, C. Albrecht, P. Alou, M. Altarelli, P. Altmann, K. Amyan, V. Anashin, E. Apostolov, K. Appel, D. Auguste, V. Ayvazyan, S. Baark, F. Babies, N. Baboi, P. Bak, V. Balandin, R. Baldinger, B. Baranasic, S. Barbanotti, O. Belikov, V. Belokurov, L. Belova, V. Belyakov, S. Berry, M. Bertucci, B. Beutner, A. Block, M. Blöcher, T. Böckmann, C. Bohm, M. Böhnert, V. Bondar, E. Bondarchuk, M. Bonezzi, P. Borowiec, C. Bösch, U. Bösenberg, A. Bosotti, R. Böspflug, M. Bousonville, E. Boyd, Y. Bozhko, A. Brand, J. Branlard, S. Briechle, F. Brinker, S. Brinker, R. Brinkmann, S. Brockhauser, O. Brovko, H. Brück, A. Brüdgam, L. Butkowski, T. Büttner, J. Calero, E. Castro-Carballo, G. Cattalanotto, J. Charrier, J. Chen, A. Cherepenko, V. Cheskidov, M. Chiodini, A. Chong, S. Choroba, M. Chorowski, D. Churanov, W. Cichalewski, M. Clausen, W. Clement, C. Cloué, J. A. Cobos, N. Coppola, S. Cunis, K. Czuba, M. Czwalinna, B. D'Almagne, J. Dammann, H. Danared, A. De Zubiaurre Wagner, A. Delfs, T. Delfs, F. Dietrich, T. Dietrich, M. Dohlus, M. Dommach, A. Donat, X. Dong, N. Doynikov, M. Dressel, M. Duda, P. Duda, H. Eckoldt, W. Ehsan, J. Eidam, F. Eints, C. Engling, U. Englisch, A. Ermakov, K. Escherich, J. Eschke, E. Saldin, M. Faesing, A. Fallou, M. Felber, M. Fenner, B. Fernandes, J. M. Fernández, S. Feuker, K. Filippakopoulos, K. Floettmann, V. Fogel, M. Fontaine, A. Francés, I. F. Martin, W. Freund, T. Freyermuth, M. Friedland, L. Fröhlich, M. Fusetti, J. Fydrych, A. Gallas, O. García, L. Garcia-Tabares, G. Geloni, N. Gerasimova, C. Gerth, P. Geßler, V. Gharibyan, M. Gloor, J. Głowinkowski, A. Goessel, Z. Gołebiewski, N. Golubeva, W. Grabowski, W. Graeff, A. Grebentsov, M. Grecki, T. Grevsmuehl, M. Gross, U. Grosse-Wortmann, J. Grünert, S. Grunewald, P. Grzegory, G. Feng, H. Guler, G. Gusev, J. L. Gutierrez, L. Hagge, M. Hamberg, R. Hanneken, E. Harms, I. Hartl, A. Hauberg, S. Hauf, J. Hauschildt, J. Hauser, J. Havlicek, A. Hedqvist, N. Heidbrook, F. Hellberg, D. Henning, O. Hensler, T. Hermann, A. Hidvégi, M. Hierholzer, H. Hintz, F. Hoffmann, M. Hoffmann, M. Hoffmann, Y. Holler, M. Hüning, A. Ignatenko, M. Ilchen, A. Iluk, J. Iversen, J. Iversen, M. Izquierdo, L. Jachmann, N. Jardon, U. Jastrow, K. Jensch, J. Jensen, M. Jeżabek, M. Jidda, H. Jin, N. Johansson, R. Jonas, W. Kaabi, D. Kaefer, R. Kammering, H. Kapitza, S. Karabekyan, S. Karstensen, K. Kasprzak, V. Katalev, D. Keese, B. Keil, M. Kholopov, M. Killenberger, B. Kitaev, Y. Klimchenko, R. Klos, L. Knebel, A. Koch, M. Koepke, S. Köhler, W. Köhler, N. Kohlstrunk, Z. Konopkova, A. Konstantinov, W. Kook, W. Koprek, M. Körfer, O. Korth, A. Kosarev, K. Kosiński, D. Kostin, Y. Kot, A. Kotarba, T. Kozak, V. Kozak, R. Kramert, M. Krasilnikov, A. Krasnov, B. Krause, L. Kravchuk, O. Krebs, R. Kretschmer, J. Kreutzkamp, O. Kröplin, K. Krzysik, G. Kube, H. Kuehn, N. Kujala, V. Kulikov, V. Kuzminych, D. La Civita, M. Lacroix, T. Lamb, A. Lancetov, M. Larsson, D. Le Pinvidic, S. Lederer, T. Lensch, D. Lenz, A. Leuschner, F. Levenhagen, Y. Li, J. Liebing, L. Lilje, T. Limberg, D. Lipka, B. List, J. Liu, S. Liu, B. Lorbeer, J. Lorkiewicz, H. H. Lu, F. Ludwig, K. Machau, W. Maciocha, C. Madec, C. Magueur, C. Maiano, I. Maksimova, K. Malcher, T. Maltezopoulos, E. Mamoshkina, B. Manschwetus, F. Marcellini, G. Marinkovic, T. Martinez, H. Martirosyan, W. Maschmann, M. Maslov, A. Matheisen, U. Mavric, J. Meißner, K. Meissner, M. Messerschmidt, N. Meyners, G. Michalski, P. Michelato, N. Mildner, M. Moe, F. Moglia, C. Mohr, S. Mohr, W. Möller, M. Mommerz, L. Monaco, C. Montiel, M. Moretti, I. Morozov, P. Morozov, D. Mross, J. Mueller, C. Müller, J. Müller, K. Müller, J. Munilla, A. Münnich, V. Muratov, O. Napoly, B. Näser, N. Nefedov, R. Neumann, R. Neumann, N. Ngada, D. Noelle, F. Obier, I. Okunev, J. A. Oliver, M. Omet, A. Oppelt, A. Ottmar, M. Oublaid, C. Pagani, R. Paparella, V. Paramonov, C. Peitzmann, J. Penning, A. Perus, F. Peters, B. Petersen, A. Petrov, I. Petrov, S. Pfeiffer, J. Pflüger, S. Philipp, Y. Pienaud, P. Pierini, S. Pivovarov, M. Planas, E. Plawski, M. Pohl, J. Polinski, V. Popov, S. Prat, J. Prenting, G. Priebe, H. Pryschelski, K. Przygoda, E. Pyata, B. Racky, A. Rathjen, W. Ratuschni, S. Regnaud-Campderros, K. Rehlich, D. Reschke, C. Robson, J. Roever, M. Roggli, J. Rothenburg, E. Rusiński, R. Rybaniec, H. Sahling, M. Salmani, L. Samoylova, D. Sanzone, F. Saretzki, O. Sawlanski, J. Schaffran, H. Schlarb, M. Schlösser, V. Schlott, C. Schmidt, F. Schmidt-Foehre, M. Schmitz, M. Schmökel, T. Schnautz, E. Schneidmiller, M. Scholz, B. Schöneburg, J. Schultze, C. Schulz, A. Schwarz, J. Sekutowicz, D. Sellmann, E. Semenov, S. Serkez, D. Sertore, N. Shehzad, P. Shemarykin, L. Shi, M. Sienkiewicz, D. Sikora, M. Sikorski, A. Silenzi, C. Simon, W. Singer, X. Singer, H. Sinn, K. Sinram, N. Skvorodnev, P. Smirnow, T. Sommer, A. Sorokin, M. Stadler, M. Steckel, B. Steffen, N. Steinhau-Kühl, F. Stephan, M. Stodulski, M. Stolper, A. Sulimov, R. Susen, J. Świerblewski, C. Sydlo, E. Syresin, V. Sytchev, J. Szuba, N. Tesch, J. Thie, A. Thiebault, K. Tiedtke, D. Tischhauser, J. Tolkiehn, S. Tomin, F. Tonisch, F. Toral, I. Torbin, A. Trapp, D. Treyer, G. Trowitzsch, T. Trublet, T. Tschentscher, F. Ullrich, M. Vannoni, P. Varela, G. Varghese, G. Vashchenko, M. Vasic, C. Vazquez-Velez, A. Verguet, S. Vilcins-Czvitkovits, R. Villanueva, B. Visentin, M. Viti, E. Vogel, E. Volobuev, R. Wagner, N. Walker, T. Wamsat, H. Weddig, G. Weichert, H. Weise, R. Wenndorf, M. Werner, R. Wichmann, C. Wiebers, M. Wiencek, T. Wilksen, I. Will, L. Winkelmann, M. Winkowski, K. Wittenburg, A. Witzig, P. Wlk, T. Wohlenberg, M. Wojciechowski, F. Wolff-Fabris, G. Wrochna, K. Wrona, M. Yakopov, B. Yang, F. Yang, M. Yurkov, I. Zagorodnov, P. Zalden, A. Zavadtsev, D. Zavadtsev, A. Zhirnov, A. Zhukov, V. Ziemann, A. Zolotov, N. Zolotukhina, F. Zummack, and D. Zybin, "A MHz-repetition-rate hard X-ray free-electron laser driven by a superconducting linear accelerator," Nat. Photonics **14**, 391–397 (2020).
[24]A. Lévy, P. Audebert, R. Shepherd, J. Dunn, M. Cammarata, O. Ciricosta, F. Deneuville, F. Dorchies, M. Fajardo, C. Fourment, D. Fritz, J. Fuchs, J. Gaudin, M. Gauthier, A. Graf, H. J. Lee, H. Lemke, B. Nagler, J. Park, O. Peyrusse, A. B. Steel, S. M. Vinko, J. S. Wark, G. O. Williams, D. Zhu, and R. W. Lee, "The creation of large-volume, gradient-free warm dense matter with an x-ray free-electron laser," Phys. Plasmas **22**, 030703 (2015).
[25]H. P. Liermann, Z. Konôpková, K. Appel, C. Prescher, A. Schropp, V. Cerantola, R. J. Husband, J. D. McHardy, M. I. McMahon, R. S. McWilliams, C. M. Pépin, J. Mainberger, M. Roeper, A. Berghäuser, H. Damker, P. Talkovski, M. Foese, N. Kujala, O. B. Ball, M. A. Baron, R. Briggs, M. Bykov, E. Bykova, J. Chantel, A. L. Coleman, H. Cynn, D. Dattelbaum, L. E. Dresselhaus-Marais, J. H. Eggert, L. Ehm, W. J. Evans, G. Fiquet, M. Frost, K. Glazyrin, A. F. Goncharov, H. Hwang, Z. Jenei, J.-Y. Kim, F. Langenhorst, Y. Lee, M. Makita, H. Marquardt, E. E. McBride, S. Merkel, G. Morard, E. F. O'Bannon, C. Otzen, E. J. Pace, A. Pelka, J. S. Pigott, V. B. Prakapenka, R. Redmer, C. Sanchez-Valle, M. Schoelmerich, S. Speziale, G. Spiekermann, B. T. Sturtevant, S. Toleikis, N. Velisavljevic, M. Wilke, C.-S. Yoo, C. Baehtz,

U. Zastrau, and C. Strohm, "Novel experimental setup for megahertz X-ray diffraction in a diamond anvil cell at the High Energy Density (HED) instrument of the European X-ray Free-Electron Laser (EuXFEL)," J. Synchrotron Radiat. **28**, 688–706 (2021).
[26]U. Zastrau, K. Appel, C. Baehtz, O. Baehr, L. Batchelor, A. Berghäuser, M. Banjafar, E. Brambrink, V. Cerantola, T. E. Cowan, H. Damker, S. Dietrich, S. Di Dio Cafiso, J. Dreyer, H.-O. Engel, T. Feldmann, S. Findeisen, M. Foese, D. Fulla-Marsa, S. Göde, M. Hassan, J. Hauser, T. Herrmannsdörfer, H. Höppner, J. Kaa, P. Kaever, K. Knöfel, Z. Konôpková, A. Laso García, H.-P. Liermann, J. Mainberger, M. Makita, E.-C. Martens, E. E. McBride, D. Möller, M. Nakatsutsumi, A. Pelka, C. Plueckthun, C. Prescher, T. R. Preston, M. Röper, A. Schmidt, W. Seidel, J.-P. Schwinkendorf, M. O. Schoelmerich, U. Schramm, A. Schropp, C. Strohm, K. Sukharnikov, P. Talkovski, I. Thorpe, M. Toncian, T. Toncian, L. Wollenweber, S. Yamamoto, and T. Tschentscher, "The high energy density scientific instrument at the European XFEL," J. Synchrotron Radiat. **28**, 1393–1416 (2021).
[27]Z. Konôpková, E. Edmund, O. B. Ball, A. Dewaele, H. Ginestet, R. J. Husband, N. Jaisle, C. Strohm, M. S. Anae, D. Antonangeli, K. Appel, M. Baron, S. Boccato, K. Buakor, J. Chantel, H. Cynn, A. P. Dwivedi, L. Ehm, K. Glazyrin, H. Graafsma, E. Koemets, T. Laurus, H. Marquardt, B. Massani, J. D. McHardy, M. I. McMahon, V. Prakapenka, J. Sztuk-Dambietz, M. Tang, T. Xie, Z. Younes, U. Zastrau, A. F. Goncharov, C. Prescher, R. S. McWilliams, G. Morard, and S. Merkel, "Observation of body-centered cubic iron above 200 Gigapascals," arXiv:2505.15397 (2025).
[28]O. B. Ball, C. Prescher, K. Appel, C. Baehtz, M. A. Baron, R. Briggs, V. Cerantola, J. Chantel, S. Chariton, A. L. Coleman, H. Cynn, H. Damker, D. Dattelbaum, L. E. Dresselhaus-Marais, J. H. Eggert, L. Ehm, W. J. Evans, G. Fiquet, M. Frost, K. Glazyrin, A. F. Goncharov, R. J. Husband, H. Hwang, N. Jaisle, Z. Jenei, J.-Y. Kim, Y. Lee, H. P. Liermann, J. Mainberger, M. Makita, H. Marquardt, E. E. McBride, J. D. McHardy, M. I. McMahon, S. Merkel, G. Morard, E. F. O'Bannon, C. Otzen, E. J. Pace, A. Pelka, C. M. Pépin, J. S. Pigott, C. Plückthun, V. B. Prakapenka, R. Redmer, S. Speziale, G. Spiekermann, C. Strohm, B. T. Sturtevant, P. Talkovski, L. Wollenweber, U. Zastrau, R. S. McWilliams, and Z. Konôpková, "Dynamic optical spectroscopy and pyrometry of static targets under optical and x-ray laser heating at the European XFEL," J. Appl. Phys. **134**, 055901 (2023).
[29]J. Meza-Galvez, N. Gomez-Perez, A. S. Marshall, A. L. Coleman, K. Appel, H. P. Liermann, M. I. McMahon, Z. Konôpková, and R. S. McWilliams, "Thermomechanical response of thickly tamped targets and diamond anvil cells under pulsed hard x-ray irradiation," J. Appl. Phys. **127**, 195902 (2020).
[30]O. B. Ball, R. J. Husband, J. D. McHardy, M. I. McMahon, C. Strohm, Z. Konôpková, K. Appel, V. Cerantola, A. L. Coleman, H. Cynn, A. Dwivedi, A. F. Goncharov, H. Graafsma, L. Q. Huston, H. Hwang, J. Kaa, J.-Y. Kim, E. Koemets, T. Laurus, X. Li, H. Marquardt, A. S. J. Méndez, S. Merkel, A. Mondal, G. Morard, V. B. Prakapenka, C. Prescher, T. R. Preston, S. Speziale, S. Stern, B. T. Sturtevant, J. Sztuk-Dambietz, N. Velisavljevic, C.-S. Yoo, U. Zastrau, Z. Jenei, H. P. Liermann, and R. S. McWilliams, "Measurement bias in self-heating x-ray free electron laser experiments from diffraction studies of phase transformation in titanium," J. Appl. Phys. **136**, 115902 (2024).
[31]A. Dewaele, V. Svitlyk, F. Bottin, J. Bouchet, and J. Jacobs, "Iron under conditions close to the $\alpha - \gamma - \varepsilon$ triple point," Appl. Phys. Lett. **112**, 201906 (2018).
[32]S. Anzellini, A. Dewaele, M. Mezouar, P. Loubeyre, and G. Morard, "Melting of iron at Earth's inner core boundary based on fast X-ray diffraction," Science **340**, 464–466 (2013).
[33]T. Komabayashi, Y. Fei, Y. Meng, and V. Prakapenka, "In-situ X-ray diffraction measurements of the $\gamma - \varepsilon$ transition boundary of iron in an internally-heated diamond anvil cell," Earth Planet. Sci. Lett. **282**, 252–257 (2009).
[34]R. Boehler, N. Von Bargen, and A. Chopelas, "Melting, thermal expansion, and phase transitions of iron at high pressures," J. Geophys. Res. **95**, 21731, https://doi.org/10.1029/JB095iB13p21731 (1990).
[35]R. Sinmyo, K. Hirose, and Y. Ohishi, "Melting curve of iron to 290 GPa determined in a resistance-heated diamond-anvil cell," Earth Planet. Sci. Lett. **510**, 45–52 (2019).
[36]T. Takahashi and W. A. Bassett, "High-pressure polymorph of iron," Science **145**, 483–486 (1964).
[37]S. Merkel, A. Lincot, and S. Petitgirard, "Microstructural effects and mechanism of bcc-hcp-bcc transformations in polycrystalline iron," Phys. Rev. B **102**, 104103 (2020).
[38]A. Dewaele, C. Denoual, S. Anzellini, F. Occelli, M. Mezouar, P. Cordier, S. Merkel, M. Véron, and E. Rausch, "Mechanism of the $\alpha - \varepsilon$ phase transformation in iron," Phys. Rev. B **91**, 174105 (2015).
[39]G. Shen, H.-K. Mao, R. J. Hemley, T. S. Duffy, and M. L. Rivers, "Melting and crystal structure of iron at high pressures and temperatures," Geophys. Res. Lett. **25**, 373–376, https://doi.org/10.1029/97GL03776 (1998).
[40]Y. Ma, M. Somayazulu, G. Shen, H.-K. Mao, J. Shu, and R. J. Hemley, "In situ X-ray diffraction studies of iron to Earth-core conditions," Phys. Earth Planet. Inter. **143–144**, 13 (2004).
[41]R. Boehler, "Temperatures in the Earth's core from melting-point measurements of iron at high static pressures," Nature **363**, 534–536 (1993).
[42]D. Zhang, J. M. Jackson, J. Zhao, W. Sturhahn, E. E. Alp, M. Y. Hu, T. S. Toellner, C. A. Murphy, and V. B. Prakapenka, "Temperature of Earth's core constrained from melting of Fe and $Fe_{0.9}Ni_{0.1}$ at high pressures," Earth Planet. Sci. Lett. **447**, 72–83 (2016).
[43]M. Hou, J. Liu, Y. Zhang, X. Du, H. Dong, L. Yan, J. Wang, L. Wang, and B. Chen, "Melting of iron explored by electrical resistance jump up to 135 GPa," Geophys. Res. Lett. **48**, e2021GL095739, https://doi.org/10.1029/2021GL095739 (2021).
[44]Z. Konôpková, W. Morgenroth, R. Husband, N. Giordano, A. Pakhomova, O. Gutowski, M. Wendt, K. Glazyrin, A. Ehnes, J. T. Delitz, A. F. Goncharov, V. B. Prakapenka, and H.-P. Liermann, "Laser heating system at the Extreme Conditions Beamline, P02.2, PETRA III," J. Synchrotron Radiat. **28**, 1747–1757 (2021).
[45]F. González-Cataldo and B. Militzer, "*Ab initio* determination of iron melting at terapascal pressures and Super-Earths core crystallization," Phys. Rev. Res. **5**, 033194 (2023).
[46]S. Balugani, J. Hernandez, N. Sévelin-Radiguet, O. Mathon, V. Recoules, J. Kas, D. Eakins, H. Doyle, A. Ravasio, and R. Torchio, "New constraints on the melting temperature and phase stability of shocked iron up to 270 GPa probed by ultrafast X-ray absorption spectroscopy," Phys. Rev. Lett. **133**, 254101 (2024).
[47]A. B. Belonoshko, J. Fu, and G. Smirnov, "Free energies of iron phases at high pressure and temperature: Molecular dynamics study," Phys. Rev. B **104**, 104103 (2021).
[48]R. Hrubiak, Y. Meng, and G. Shen, "Experimental evidence of a body centered cubic iron at the Earth's core condition," arXiv:1804.05109 (2018).
[49]D. Alfè, M. J. Gillan, and G. D. Price, "The melting curve of iron at the pressures of the Earth's core from *ab initio* calculations," Nature **401**, 462–464 (1999).
[50]A. Allahgholi, J. Becker, A. Delfs, R. Dinapoli, P. Göttlicher, H. Graafsma, D. Greiffenberg, H. Hirsemann, S. Jack, A. Klyuev, H. Krüger, M. Kuhn, T. Laurus, A. Marras, D. Mezza, A. Mozzanica, J. Poehlsen, O. Shefer Shalev, I. Sheviakov, B. Schmitt, J. Schwandt, X. Shi, S. Smoljanin, U. Trunk, J. Zhang, and M. Zimmer, "Megapixels @ Megahertz—The AGIPD high-speed cameras for the European XFEL," Nucl. Instrum. Methods Phys. Res. Sect. A **942**, 162324 (2019).
[51]J. D. McHardy, "X-ray free-electron laser heating and structural studies in the diamond anvil cell," Ph.D. thesis (University of Edinburgh, 2024).
[52]N. Kujala, W. Freund, J. Liu, A. Koch, T. Falk, M. Planas, F. Dietrich, J. Laksman, T. Maltezopoulos, J. Risch, F. Dall'Antonia, and J. Grünert, "Hard x-ray single-shot spectrometer at the European X-ray Free-Electron Laser," Rev. Sci. Instrum. **91**, 103101 (2020).
[53]T. Maltezopoulos, F. Brinker, F. Dietrich, W. Freund, J. Grünert, U. F. Jastrow, N. Kujala, J. Laksman, J. Liu, K. Tiedtke, and T. Tschentscher, "Hard X-ray operation of X-ray gas monitors at the European XFEL," J. Synchrotron Radiat. **31**, 681–689 (2024).
[54]C. Prescher and V. B. Prakapenka, "*DIOPTAS*: A program for reduction of two-dimensional X-ray diffraction data and data exploration," High Pressure Res. **35**, 223–230 (2015).

[55]O. T. Lord, I. G. Wood, D. P. Dobson, L. Vočadlo, W. Wang, A. R. Thomson, E. T. Wann, G. Morard, M. Mezouar, and M. J. Walter, "The melting curve of Ni to 1 Mbar," Earth Planet. Sci. Lett. **408**, 226–236 (2014).
[56]N. Jaisle, D. Cébron, Z. Konôpková, R. J. Husband, C. Prescher, V. Cerantola, A. Dwivedi, J. M. Kaa, K. Appel, K. Buakor, O. B. Ball, R. S. McWilliams, C. Strohm, M. Nakatsutsumi, U. Zastrau, C. Baehtz, M. Anna Baron, E. Edmund, J. Biswas, J. D. McHardy, B. T. Sturtevant, L. Ehm, A. F. Goncharov, M. I. McMahon, J. Buchen, H. Cynn, E. J. Pace, H.-P. Liermann, D. T. Sneed, S. C. Cooper, M. Anae, J. Kim, Z. Wu, Y. Lee, H. J. Hwang, T. Kim, J. Choi, J. Lee, S. Merkel, J. Chantel, E. G. Koemets, H. Marquardt, V. B. Prakapenka, S. Chariton, E. Shevchenko, G. Fiquet, A. D. Rosa, M. Mezouar, G. Garbarino, and G. Morard, "MHz free electron laser x-ray diffraction and modeling of pulsed laser heated diamond anvil cell," J. Appl. Phys. **134**, 095904 (2023).
[57]N. Jaisle, "Contraindre la fusion partielle dans les intérieurs planétaires en combinant les approches numériques et expérimentales," Ph.D. thesis (Université Grenoble-Alpes, 2024).
[58]D. Zhou, J. Dong, Y. Si, F. Zhu, and J. Li, "Melting curve of potassium chloride from in situ ionic conduction measurements," Minerals **10**, 250 (2020).
[59]R. J. Husband, H. P. Liermann, J. D. McHardy, R. S. McWilliams, A. F. Goncharov, V. B. Prakapenka, E. Edmund, S. Chariton, Z. Konôpková, C. Strohm, C. Sanchez-Valle, M. Frost, L. Andriambariarijaona, K. Appel, C. Baehtz, O. B. Ball, R. Briggs, J. Buchen, V. Cerantola, J. Choi, A. L. Coleman, H. Cynn, A. Dwivedi, H. Graafsma, H. Hwang, E. Koemets, T. Laurus, Y. Lee, X. Li, H. Marquardt, A. Mondal, M. Nakatsutsumi, S. Ninet, E. Pace, C. Pepin, C. Prescher, S. Stern, J. Sztuk-Dambietz, U. Zastrau, and M. I. McMahon, "Phase transition kinetics of superionic H_2O ice phases revealed by Megahertz X-ray free-electron laser-heating experiments," Nat. Commun. **15**, 8256 (2024).
[60]A. Dewaele, P. Loubeyre, F. Occelli, M. Mezouar, P. I. Dorogokupets, and M. Torrent, "Quasihydrostatic equation of state of iron above 2 Mbar," Phys. Rev. Lett. **97**, 215504 (2006).
[61]T. Komabayashi and Y. Fei, "Internally consistent thermodynamic database for iron to the Earth's core conditions," J. Geophys. Res. **115**, B03202, https://doi.org/10.1029/2009JB006442 (2010).
[62]T. Komabayashi, "Thermodynamics of melting relations in the system Fe-FeO at high pressure: Implications for oxygen in the Earth's core," J. Geophys. Res.: Solid Earth **119**, 4164–4177, https://doi.org/10.1002/2014JB010980 (2014).
[63]C. E. Yen, Q. Williams, and M. Kunz, "Thermal pressure in the laser-heated diamond anvil cell: A quantitative study and implications for the density versus mineralogy correlation of the mantle," J. Geophys. Res.: Solid Earth **125**, e2020JB020006, https://doi.org/10.1029/2020JB020006 (2020).
[64]G. Morard, D. Andrault, N. Guignot, J. Siebert, G. Garbarino, and D. Antonangeli, "Melting of Fe–Ni–Si and Fe–Ni–S alloys at megabar pressures: Implications for the core–mantle boundary temperature," Phys. Chem. Miner. **38**, 767–776 (2011).
[65]J. M. Brown and R. B. McQueen, "Phase transitions, Grüneisen parameter, and elasticity for shocked iron between 77 GPa and 400 GPa," J. Geophys. Res. **91**, 7485–7494, https://doi.org/10.1029/JB091iB07p07485 (1986).
[66]J. H. Nguyen and N. C. Holmes, "Melting of iron at the physical conditions of the Earth's core," Nature **427**, 339–342 (2004).
[67]A. Kavner and T. S. Duffy, "Pressure–volume–temperature paths in the laser-heated diamond anvil cell," J. Appl. Phys. **89**, 1907–1914 (2001).
[68]J. M. Brown and R. G. McQueen, "Melting of iron under core conditions," Geophys. Res. Lett. **7**, 533–536, https://doi.org/10.1029/GL007i007p00533 (1980).
[69]S. Singh, R. Briggs, M. G. Gorman, L. X. Benedict, C. J. Wu, S. Hamel, A. L. Coleman, F. Coppari, A. Fernandez-Pañella, C. McGuire, M. Sims, J. K. Wicks, J. H. Eggert, D. E. Fratanduono, and R. F. Smith, "Structural study of hcp and liquid iron under shock compression up to 275 GPa," Phys. Rev. B **108**, 184104 (2023).
[70]S. Turneaure, S. Sharma, and Y. Gupta, "Crystal structure and melting of Fe shock compressed to 273 GPa: *In situ* X-ray diffraction," Phys. Rev. Lett. **125**, 215702 (2020).
[71]N. Jourdain, L. Lecherbourg, V. Recoules, P. Renaudin, and F. Dorchies, "Ultrafast thermal melting in nonequilibrium warm dense copper," Phys. Rev. Lett. **126**, 065001 (2021).
[72]S. Zhang, A. Panjwani, P. Xiao, M. Ghosh, T. Ogitsu, Y. Ping, and S. X. Hu, "Thermally induced structural competitiveness and metastability of body-centered-cubic iron under nonequilibrium conditions," Phys. Rev. B **111**, 224106 (2025).
[73]T. Sakai, S. Takahashi, N. Nishitani, I. Mashino, E. Ohtani, and N. Hirao, "Equation of state of pure iron and $Fe_{0.9}Ni_{0.1}$ alloy up to 3 Mbar," Phys. Earth Planet. Inter. **228**, 114–126 (2014).
[74]F. Miozzi, J. Matas, N. Guignot, J. Badro, J. Siebert, and G. Fiquet, "A new reference for the thermal equation of state of iron," Minerals **10**, 100 (2020).
[75]R. Hrubiak, J. S. Smith, and G. Shen, "Multimode scanning X-ray diffraction microscopy for diamond anvil cell experiments," Rev. Sci. Instrum. **90**, 025109 (2019).
[76]B. L. Henke, E. M. Gullikson, and J. C. Davis, "X-ray interactions: Photoabsorption, scattering, transmission, and reflection at $E = 50 - 30\,000$ eV, $Z = 1 - 92$," At. Data Nucl. Data Tables **54**(2), 181–342 (1993).
[77]A. Dewaele, A. B. Belonoshko, G. Garbarino, F. Occelli, P. Bouvier, M. Hanfland, and M. Mezouar, "High-pressure–high-temperature equation of state of KCl and KBr," Phys. Rev. B **85**, 214105 (2012).
[78]N. Tsujino, Y. Nishihara, Y. Nakajima, E. Takahashi, K.-I. Funakoshi, and Y. Higo, "Equation of state of γ-Fe: Reference density for planetary cores," Earth Planet. Sci. Lett. **375**, 244–253 (2013).
[79]Y. Kuwayama, G. Morard, Y. Nakajima, K. Hirose, A. Q. R. Baron, S. I. Kawaguchi, T. Tsuchiya, D. Ishikawa, N. Hirao, and Y. Ohishi, "Equation of state of liquid iron under extreme conditions," Phys. Rev. Lett. **124**, 165701 (2020).
[80]Z. Konôpková, R. S. McWilliams, N. Gómez-Pérez, and A. F. Goncharov, "Direct measurement of thermal conductivity in solid iron at planetary core conditions," Nature **534**, 99–101 (2016).
[81]J. Li, Q. Wu, J. Li, T. Xue, Y. Tan, X. Zhou, Y. Zhang, Z. Xiong, Z. Gao, and T. Sekine, "Shock melting curve of iron: A consensus on the temperature at the Earth's inner core boundary," Geophys. Res. Lett. **47**, e2020GL087758, https://doi.org/10.1029/2020GL087758 (2020).
[82]P. Krishna and D. Pandey, "5 close-packed structures," International Union of Crystallography Commission on Crystallographic Teaching, First Series pamphlets, No. 5 (1981).
[83]F. Frey and H. Boysen, "Disorder in cobalt single crystals," Acta Crystallogr. Sect. A **37**, 819–826 (1981).
[84]S. Merkel, G. Morard, E. Edmund, H. Ginestet, Z. Konôpková, M. Anae, D. Antonangeli, K. Appel, O. Ball, M. Baron, S. Boccato, K. Buakor, J. Chantel, H. Cynn, A. Dewaele, A. Dwivedi, L. Ehm, K. Glazyrin, A. Goncharov, H. Graafsma, R. Husband, N. Jaisle, E. Koemets, T. Laurus, H. Marquardt, B. Massani, J. McHardy, M. McMahon, S. McWilliams, V. Prakapenka, C. Prescher, C. Strohm, S.-D. Jolanta, M. Tang, T. Xie, Z. Younes and U. Zastrau (2025). "EuXFEL #3063 experiment on iron and iron alloys under planetary cores conditions," Zenodo. https://zenodo.org/records/17950889